BIOPHYSICS

Microtubule-binding core of the tau protein

Nadia El Mammeri, Aurelio J. Dregni, Pu Duan, Harrison K. Wang, Mei Hong*

The protein tau associates with microtubules to maintain neuronal health. Posttranslational modifications of tau interfere with this binding, leading to tau aggregation in neurodegenerative disorders. Here, we use solid-state nuclear magnetic resonance (NMR) to investigate the structure of the microtubule-binding domain of tau. Wild-type tau that contains four microtubule-binding repeats and a pseudorepeat R′ is studied. Complexed with taxol-stabilized microtubules, the immobilized residues exhibit well-resolved two-dimensional spectra that can be assigned to the amino-terminal region of R4 and the R′ domain. When tau coassembles with tubulin to form unstable microtubules, the R′ signals remain, whereas the R4 signals disappear, indicating that R′ remains immobilized, whereas R4 becomes more mobile. Therefore, R′ outcompetes the other four repeats to associate with microtubules. These NMR data, together with previous cryo–electron microscopy densities, indicate an extended conformation for microtubule-bound R′. R′ contains the largest number of charged residues among all repeats, suggesting that charge-charge interaction drives tau-microtubule association.

INTRODUCTION

Microtubules (MTs) constitute part of the cytoskeleton of eukaryotic cells and function in cell division and intracellular trafficking. Assembled from 13 protofilaments of α- and β-tubulin dimers, these hollow cylinders can rapidly grow and shrink in length via a guanosine 5′-triphosphate (GTP)–regulated process (Fig. 1A) (*1*). In neurons, MTs are mainly stabilized by the intrinsically disordered protein tau (*2*). In adult human brains, tau mainly distributes into axons, where it stabilizes MTs, promotes their assembly, and regulates their dynamic instability (*3*). Tau may also regulate axonal transport by interacting with motor proteins. However, hyperphosphorylation and acetylation of tau weaken this interaction (*4*), causing tau to aggregate into amyloid fibrils. The resulting neurofibrillary tangles are the hallmark of a number of neurodegenerative disorders such as Alzheimer's disease, chronic traumatic encephalopathy, and progressive supranuclear palsy (*3*, *5*–*8*). Elucidating the structure and dynamics of the tau domain that binds MTs is therefore important for understanding both the physiological function of tau and the pathogenesis of many neurodegenerative diseases. Tau contains an N-terminal projection domain (residues 1 to 150), a proline (Pro)–rich domain (residues 151 to 243), a MT-interacting region with either three or four 31-residue repeats (residues 244 to 368), a weakly homologous pseudorepeat R′ (residues 369 to 399) (*9*), and a C-terminal domain (residues 400 to 441) (Fig. 1B). All repeats are thought to bind with MTs, as suggested, for example, by the loss of solution nuclear magnetic resonance (NMR) signals of MT-bound tau (*10*). Although many biophysical studies have probed the MT interactions of tau (*11*–*13*), a near-atomic view of the bound complex was reported only recently using cryo–electron microscopy (cryo-EM) (*14*). The electron density maps of tubulin coassembled with an excess amount of wild-type tau show a continuous extended ribbon lying on the crest of the tubule protofilaments. However, at a resolution of 4.1 to 6.5 Å, these maps do not resolve the precise domain of tau that contacts the MT surface. Instead, higher-resolution maps of chimeric tau constructs that contain either four copies of the R1 repeat or four copies of the R2 repeat were obtained. These maps were modeled using Rosetta and were found to best match a 12-residue segment in the R1 domain and a 27-residue segment in the R2 domain, respectively. These results were interpreted as either R1 and R2 repeats bind to MTs with the highest affinity or all four repeats of tau bind in tandem to the MT surface. However, these binding models have not been tested in full-length wild-type tau.

RESULTS

To determine the relative affinity of all five repeats in native tau for MTs and to investigate whether the bound segment varies with MT stability, we co-sedimented wild-type recombinant tau with MTs and examined the complex using solid-state NMR spectroscopy (*15*–*17*). We prepared three samples in which 10 or 5 μM of tau was mixed with preformed and taxol-stabilized MTs at a concentration of 10 μM tubulin heterodimer. In a fourth sample, tubulin was co-assembled with twofold excess tau without stabilizing agents to form dynamically unstable MTs. Among the three taxol-stabilized samples, one contained full-length 0N4R tau, while the other two contained different concentrations of a shorter construct, P2R tau (residues 198 to 399), which includes the P2 domain, R1 to R4 repeats, and the pseudorepeat R′ (Fig. 1B).

We measured dipolar coupling–based magic-angle spinning (MAS) solid-state NMR spectra to detect MT-immobilized tau residues and J coupling–based spectra to detect highly mobile residues. Binding of equimolar amounts of full-length 0N4R or P2R tau to preformed MTs (both at 10 μM) yielded long, straight, and ~38-nm-wide tubules that are stable for ~10 days at 4°C (Fig. 1C and fig. S1A). The two-dimensional (2D) ^{15}N-^{13}Cα (NCα) correlation spectrum of P2R tau (1:1 tubulin dimer:tau) shows ~45 well-resolved peaks with narrow linewidths of 0.5 to 0.8 parts per million (ppm) for ^{13}C and 0.9 to 1.1 ppm for ^{15}N (Fig. 1D). Because this dipolar experiment preferentially detects immobilized residues, these narrow linewidths indicate that the MT-bound domain in P2R tau has a rigid and well-ordered structure. MT-bound full-length 0N4R tau exhibits a similar 2D NCα spectrum, indicating that full-length tau has a similar immobilized binding domain as P2R tau on preformed MTs (fig. S2). Thus, the N-terminal projection domain and the C-terminal domain, which are absent in P2R tau, do not cause substantial changes to the identity and the conformation of the MT-binding domain.

Department of Chemistry, Massachusetts Institute of Technology, 170 Albany Street, Cambridge, MA 02139, USA.
*Corresponding author. Email: meihong@mit.edu

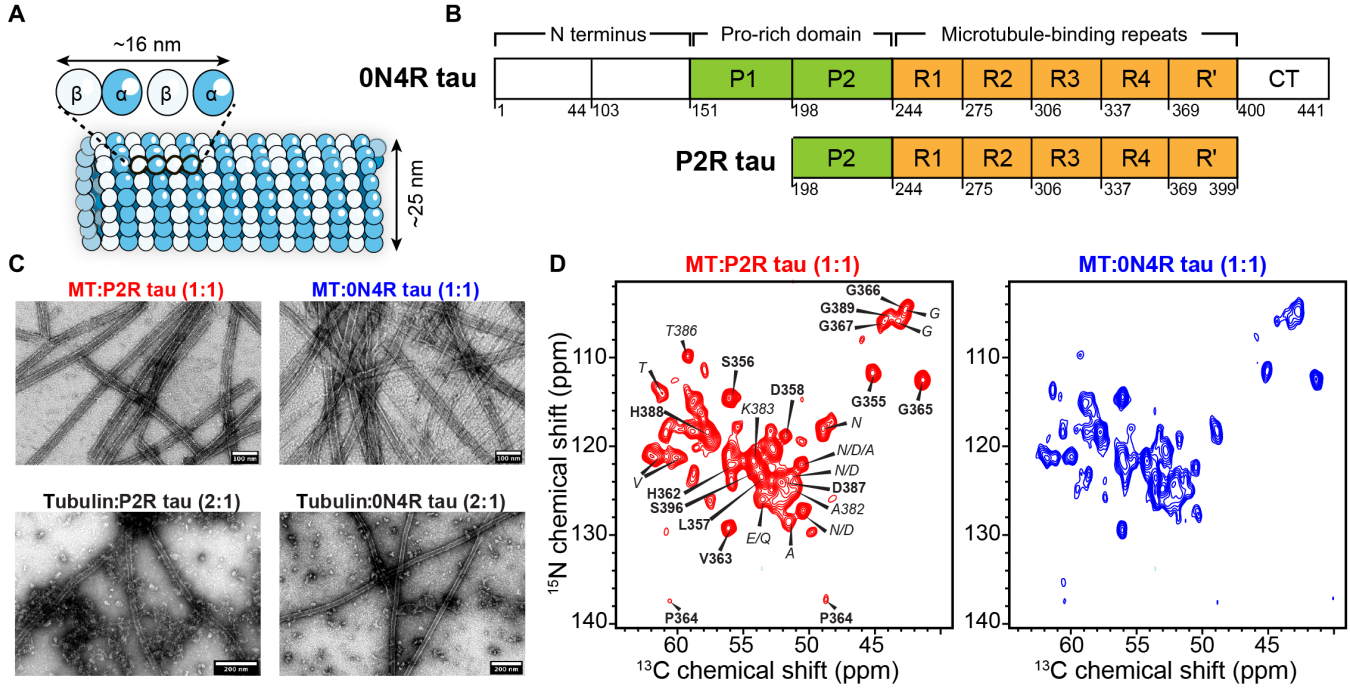

Fig. 1. 0N4R tau and P2R tau bind MTs with specific interactions. (**A**) Schematic of MTs composed of α- and β-tubulin heterodimers. (**B**) Amino acid sequence domains in 0N4R tau and P2R tau. (**C**) Negative-stain transmission electron microscopy (TEM) images of preformed taxol-stabilized MTs with bound tau (top row) and tubulin-tau coassembly without stabilizing agents (bottom row). Tau-bound stabilized MTs appear as homogeneous and straight tubules (top row; scale bars, 100 nm), while tubulin-tau coassembly gives a mixture of straight MTs with a small amount of unassembled tubulin (bottom row; scale bars, 200 nm). All four samples contain 10 μM tubulin heterodimers. (**D**) 2D NCα spectra of ^{13}C, ^{15}N-labeled P2R tau (left) and 0N4R tau (right) bound to stabilized MTs at a 1:1 molar ratio of tubulin dimer:tau. The P2R tau spectrum can be sequentially assigned to R′ and R4 residues (bold). Residue-type or ambiguous assignments are italicized. 0N4R tau exhibits a similar spectral pattern, indicating that the MT-binding domain is similar to P2R tau.

To facilitate the assignment of the MT-immobilized tau domain, we also investigated the dynamic residues of P2R tau in the MT-bound complex. 1D and 2D ^{1}H-^{13}C insensitive nuclei enhanced by polarization transfer (INEPT) spectra of P2R tau (Fig. 2, A and B, and fig. S3D) show many sharp signals at random coil chemical shifts (table S1), indicating the presence of highly mobile side chains and some backbones in MT-bound tau. We detected the Cβ signal of a Pro-preceding Ala, A(P), and the Cε peak of a Met in the INEPT spectrum, with an intensity ratio of ~1.0 (table S2). There is only a single A(P) residue (Ala^{246}) and a single Met (Met^{250}) residue in P2R tau, both located at the beginning of the R1 domain (Fig. 2D). Therefore, the N-terminal region of R1 is highly mobile. We also observed an INEPT peak for Pro-preceding Ser residues, whose intensity is about three times the intensities of the A(P) and Met peaks. There are only four Pro-preceding Ser residues in P2R tau, three in the P2 domain and one near the C terminus of the R′ domain. This large intensity cannot be all attributed to the single S(P) residue in R′; therefore, the P2 segment must contain highly dynamic Pro-preceding Ser residues. Last, among the small number of aromatic residues in P2R tau, we detected the INEPT signals of His side chains (Fig. 2, A and B), which occur in all five repeats, but no signals of Tyr and Phe side chains, which occur in R3, R4, and R′. Therefore, the Tyr and Phe residues and their immediate neighboring residues in R3, R4, and R′ are not highly mobile in MT-bound tau. These observations indicate that the most mobile residues in MT-bound P2R tau are concentrated in the N-terminal region of the protein, including the P2 and R1 segments, whereas the C-terminal portion of the protein is more immobilized.

The localization of the most dynamic domain of MT-bound tau to the Pro-rich N-terminal portion of the protein facilitated the identification of the immobilized segment of MT-bound P2R tau. A 2D ^{13}C-^{13}C (CC) spin diffusion correlation spectrum (Fig. 2C) resolved ~35 spin systems, among which more than two Ala, two His, and one Phe/Tyr residues are observed. Ala residues that do not precede Pro only occur in P2 and R′ (Fig. 2, D and E). Because the Pro-rich domain contains many high mobile residues, these rigid Ala's are most likely located in the R′ domain. We also detected Tyr and Phe signals in the 2D CC spectrum, supporting the conclusion that the R3, R4, and R′ domains in the C-terminal half of P2R tau are more immobilized than that in the N-terminal half of the protein. To sequentially assign these immobilized residues, we analyzed the 2D NCα and ^{15}N-^{13}CO (NCO) correlation spectra of P2R tau (Fig. 1D) and supplemented these with the spectra of 0N4R tau (fig. S6). Although sensitivity limitations of these larger complexes prohibit 3D correlation experiments, the combination of 2D NCα, NCO, and 2D CC spectra (fig. S4) allowed us to sequentially assign 14 residues unambiguously and five residues with partial ambiguity (table S3). Among the assigned immobilized residues, the most N-terminal segment is the ^{354}IGSLD^{358} motif in the R4 domain. A unique triplet ^{387}DHG^{389} can be assigned, providing direct evidence of the involvement of the R′ in binding the MT. The 2D NCα spectrum resolved at least six Gly resonances, five of which can be assigned and three of which belong to a contiguous HVPGGG segment. There are only two HVPGGG motifs in P2R tau, one in the R4 domain and the other in the R2. Because the electron densities of MT-bound tau are

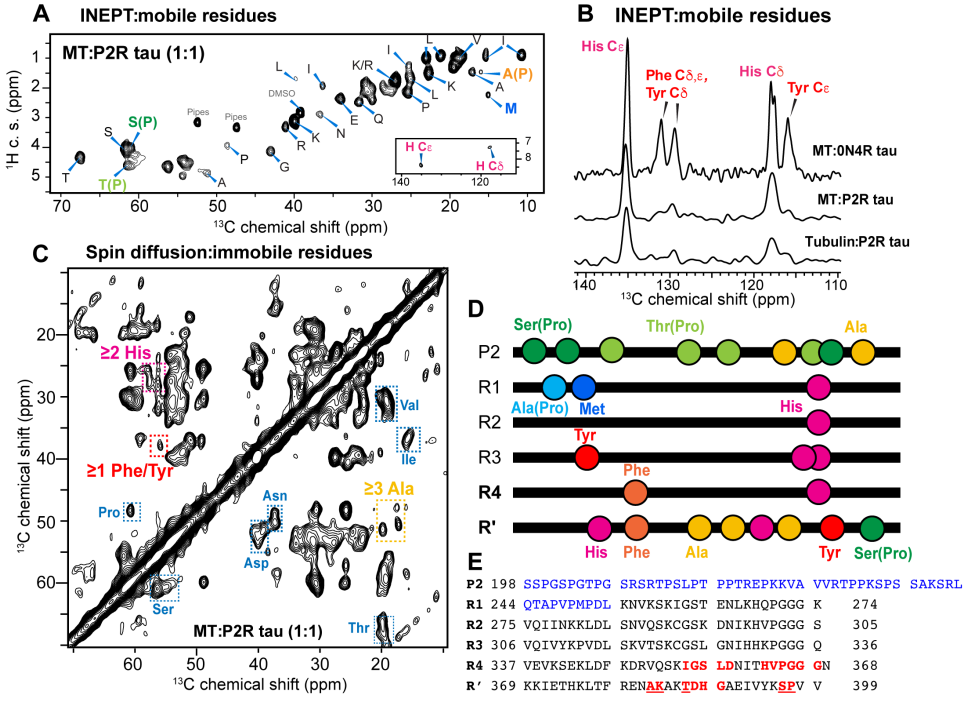

Fig. 2. MT-bound tau contains dynamic P2 and R1 domains and immobilized R′ and R4 domains. (**A**) 2D ^{1}H-^{13}C INEPT spectrum detects the dynamic residues in MT-bound P2R tau (1:1). The signals of Pro Cβ-preceding Ala, A(P), and Met Cε are assigned in bold. The aromatic region of the spectrum (inset) shows only His signals but no Phe and Tyr signals. c. s., chemical shift. (**B**) Aromatic region of the ^{13}C INEPT spectra of MT-bound 0N4R tau (1:1), MT-bound P2R tau (1:1), and tubulin coassembled with P2R tau (1:2). Only His signals are observed in P2R tau, while His, Phe, and Tyr signals are all observed in 0N4R tau due to the presence of the mobile N-terminal domain. (**C**) A 50-ms 2D CC spin diffusion spectrum of MT-bound P2R tau. Cross peaks for Ser, Pro, Thr, Ala, Val, Ile, His, and Phe/Tyr are observed (rectangles). (**D**) Location of key residues that identify the mobile and immobile segments in MT-bound tau. R′ is the only domain that contains Ala, His, Tyr, and Phe. P2 and R1 are the only domains that contain both A(P) and Met. (**E**) Amino acid sequence of P2R tau. The sequentially assigned immobilized residues lie in the R4 and R′ domains (red: unambiguously assigned residues; underlined residues: assignment with partial ambiguity). The INEPT-detected highly dynamic residues are concentrated in the Pro-rich P2 domain and the beginning of the R1 domain (shown in blue).

continuous (*13*, *14*), with rigid R4 and R′ segments already assigned in these dipolar spectra, we attribute these Pro and Gly signals to the ^{362}HVPGGG^{367} motif in the R4 domain (Fig. 2E). This assignment is also consistent with the fact that the R2 domain lacks Ala, Phe/Tyr, and Thr residues, which exhibit clear dipolar correlation signals, whereas the R4-R′ domains contain these residue types. The measured chemical shifts of the immobilized residues (table S3) indicate β strand conformation for the Ile^{354}-Gly^{367} segment in R4 and an extended conformation for the Ala^{382}-Pro^{397} segment in R′ (fig. S5). Full-length 0N4R tau displays a similar 2D NCα spectrum as P2R tau (Fig. 1D), but with lower intensities. Joint analysis of the NCα spectrum with N(CO)Cα and N(CA)CB spectra (fig. S6) indicates that the same R4-R′ domain is immobilized in the full-length protein.

In neurons, tau is present at two- to fivefold lower concentrations (5 to 10 μM) than tubulin (up to ~23 μM) (*18*). To assess whether the NMR spectra of the 1:1 complex reflect specific interactions of tau with MTs, we diluted P2R tau by twofold and measured solid-state NMR spectra. The 2D CC and NCα spectra of this 1:0.5 (tubulin dimer:tau) complex exhibit the same chemical shifts as the 1:1 sample (fig. S7), indicating that the immobilization of R4-R′ is due to specific interactions rather than nonspecific crowding. The INEPT spectrum of the 1:0.5 complex has threefold higher Met Cε intensity than the A(P) Cβ intensity, suggesting that the P2-R1 region has become more mobile at lower tau concentrations. Water-edited spectra of the 1:0.5 MT-bound P2R tau sample show low water-transferred intensities (fig. S8), indicating that the MT-anchored R4-R′ region is well protected from water (*19*–*21*). This dehydration is independent of the tubulin:tau molar ratio, suggesting that the dynamic P2 and R1 domains sequester the R4-R′ region from water.

To investigate whether the conformation and dynamics of bound tau depend on the stability of the MTs, we incubated (at 37°C) and co-sedimented tubulin with a moderate excess of P2R tau (1:2 tubulin dimer:tau) in the absence of taxol (figs. S1 and S3). This coassembly gives rise to less stable MTs compared to taxol-stabilized samples, thus mimicking the dynamic end of the MT (*22*). The 2D NCα spectrum of this coassembled sample shows lower sensitivity and a smaller number of peaks compared to tau bound to taxol-stabilized MTs (Fig. 3A). In particular, the PGGG signals disappeared, indicating that the C terminus of R4 has become more disordered. Consistently, the ^{15}N spectrum of the coassembled sample shows that the Gly signals are preferentially broadened compared to the taxol-stabilized MT-tau complex (Fig. 3C). Despite the increased dynamic disorder, characteristic chemical shifts of Arg, Ala, Thr, and Asp/Asn residues are observed in the 2D CC dipolar correlation spectrum and the NCα spectrum (Fig. 3, A and B, and fig. S9A). The only domain in tau that contains all these residue types is R′. Moreover, Tyr/Phe signals are still missing in the INEPT spectra (fig. S9B). Therefore, R′ remains to be the tau binding domain for dynamically unstable MTs. To verify the dynamics of these tau samples, we measured ^{13}C-^{1}H dipolar couplings (Fig. 4). The backbone Cα sites of tau bound to

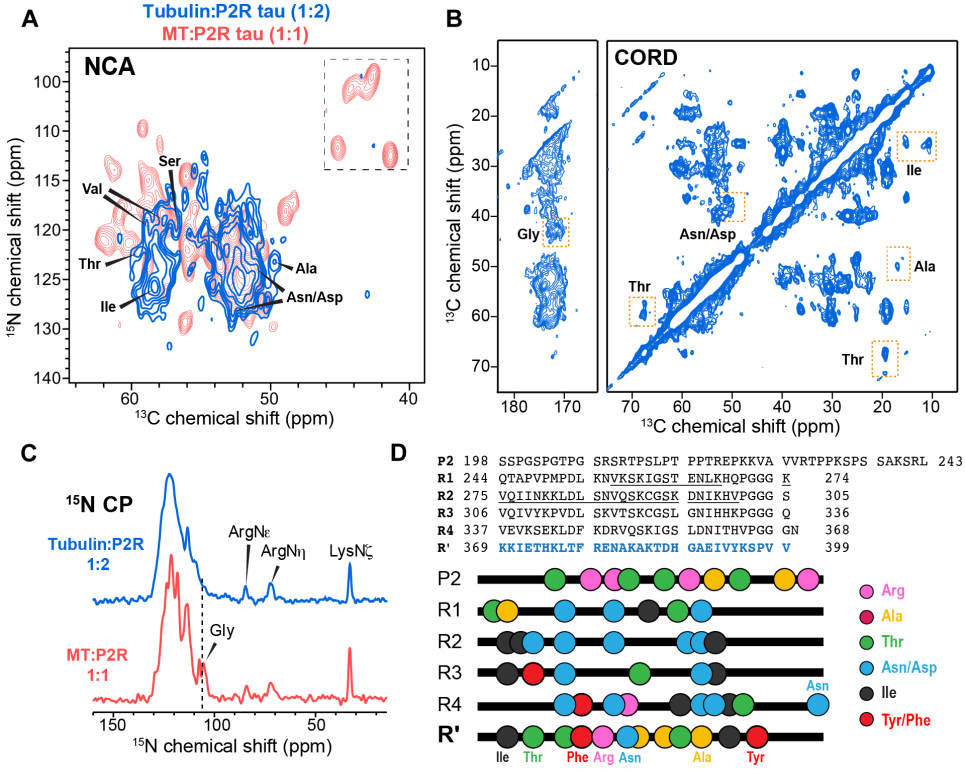

Fig. 3. R′ binds both dynamically unstable MTs. (**A**) 2D NCα spectrum of tubulin-tau (1:2) coassembly (blue), overlaid with the spectrum of taxol-stabilized MT-P2R tau (1:1) complex (red). (**B**) 2D CC correlation spectrum of tubulin-tau coassembly. Joint analysis of the two 2D spectra allows assignment of the immobilized residues. Thr, Asn, Asp, Ala, and Ile signals are observed. (**C**) ^{15}N CP spectra of P2R tau bound to unstable (top) and stabilized (bottom) microtubules. Arginine side-chain signals are detected in both spectra, indicating that some Arg side chains are immobilized by the MTs. The Gly ^{15}N signals are broadened in the coassembled sample relative to the taxol-stabilized sample. (**D**) Amino acid sequence of P2R tau and the location of key residue types that identify the immobilized segment in the tubulin:tau coassembly. R′ is the only segment that contains all residue types (Ala, Arg, Thr, Ile, Tyr/Phe, and Asp/Asn) in the dipolar spectra. The cryo-EM reported MT-bound R1 and R2 segments in chimeric tau constructs are underlined.

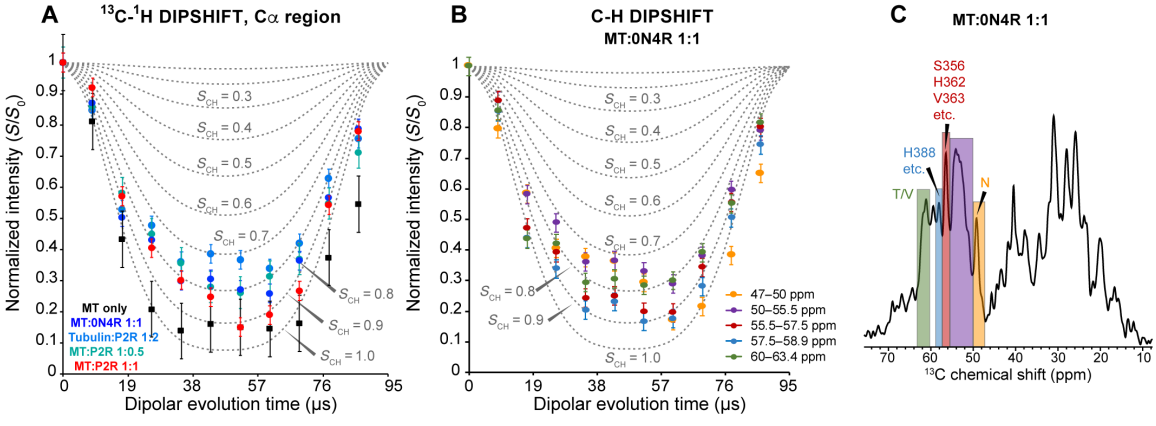

Fig. 4. MT-bound tau exhibits heterogeneous dynamics. (**A**) ^{13}C-^{1}H dipolar-doubled DIPSHIFT data (colored symbols) of MT-bound tau and MT (black symbols) alone. The spectra were measured under 10.5-kHz MAS using 70-μs CP. The intensities for the Cα region (50 to 63 ppm) were integrated and compared with simulated DIPSHIFT curves (dotted lines) for C-H dipolar order parameters (S_{CH}) of 0 to 1.0. All tau samples bound to taxol-stabilized MTs exhibit similar Cα-Hα dipolar dephasing that corresponds to S_{CH} values between 0.8 and 0.9, whereas the tubulin-tau coassembled sample (marine blue) exhibits a smaller S_{CH} of ~0.70, indicating that tau is more mobile when complexed to unstable microtubules. The MT itself exhibits the largest S_{CH} of ~0.95, indicating that it is more rigid than tau. (**B**) ^{13}C-^{1}H doubled DIPSHIFT data (symbols) of the MT:0N4R tau (1:1) sample for different regions of the spectra. All regions show S_{CH} values of 0.7 to 0.9. (**C**) First slice of the 2D DIPSHIFT spectrum of MT-bound 0N4R tau (1:1) and the regions analyzed in (B). Some peak assignments are shown.

taxol-stabilized MTs show order parameters (S_{CH}) of 0.8 to 0.9, irrespective of the binding stoichiometry (1:1 or 1:0.5). In comparison, the tubulin coassembled tau exhibits a smaller S_{CH} value of ~0.7, indicating larger motional amplitudes. Therefore, the dynamically unstable MTs increase the mobility of bound tau compared to taxol-stabilized MTs.

Previous studies using saturation transfer NMR and cryo-EM found that tau is centered on the α-tubulin subunit of MTs (*23*). If fully extended, then the 45 residue R4-R′ segment that contains all sequentially assigned immobilized residues (Fig. 2E) would span a length of ~15 nm, or two tubulin dimers, each of which is ~8 nm long (*24*). However, the current data that both the 1:1 and 1:0.5 complexes (tubulin dimer to tau) give similar NMR spectra and co-sediment similarly imply that each tau binds one tubulin dimer instead of two (*10*, *13*). Because the R′ domain already spans a tubulin dimer, this suggests that the rest of the protein progressively detaches from the MT surface (Fig. 5A). In the tubulin-tau coassembled complex, R4 is more mobile than the R′ domain (Fig. 3A), supporting the view that R′ has higher affinity to MTs than R4. This conclusion is also consistent with the cryo-EM data of a chimeric R2-replicated tau (vide infra), which show continuous electron densities that match ~27 residues but not more (*14*). These stoichiometric and geometric constraints, together with the previously reported electron density maps, suggest that, outside the R4-R′ regions, R2, R1, and P2 become increasingly dynamic and spaced away from the MT surface (Fig. 5A). In this way, these N-terminal segments might serve to recruit additional tubulin dimers for polymerization (*11*).

To obtain more information about the conformation of the MT-binding R′ in wild-type tau, we conducted homology modeling of R′ by fitting it into cryo-EM maps of MT-bound tau (*14*). The cryo-EM map of wild-type full-length tau (EMD-7522) shows continuous electron densities (Fig. 5B), but its resolution of 4.1 Å was not sufficient to permit direct identification of the bound segment. Instead, a higher-resolution (3.9 Å) map (EMD-7771) of a chimeric tau construct that contains four copies of R2 (P2-R2-R2-R2-R2-R′), which has similar shape and is indistinguishable from the wild-type tau densities, was modeled using Rosetta (*25*). This analysis found that a 27-residue segment in R2, spanning Lys^{274}-Val^{300}, binds the MT. We adopted the same approach for the R′ domain by first modeling it to fit the cryo-EM map of the chimeric R2 × 4 tau (EMD-7771). We generated 100 models of each of the seven possible 27-residue segments between G367 and V399 through refinement with Rosetta (fig. S10, A and B). The five lowest energy structures for each registry were used to assess the fit to the electron density by Rosetta energy and the binding affinity by PRODIGY (fig. S10, C to E) (*26*). We found that the Lys^{369}-Lys^{395} segment in R′ gives the best Rosetta score and the best PRODIGY score. When this segment was inserted into the density map of wild-type full-length tau (EMD-7522), we found good agreement (fig. S11). The torsion angles of this Rosetta-refined R′ segment also agree with the chemical shift–derived torsion angles (fig. S5C), supporting the conclusion that this is the most likely MT-binding core in wild-type tau.

DISCUSSION

These NMR results indicate that the imperfect fifth repeat, R′, is the domain in wild-type tau that binds both stabilized and unstable MTs with the highest affinity (Fig. 5A). Even when the tau concentration is lowered (1:0.5 tubulin dimer:tau) to leave vacant tubulin dimers, the similarity of the dipolar NMR spectra with the spectra of the 1:1 complex (fig. S7) indicates that no other repeats are immobilized sufficiently to give dipolar correlation signals. Nor is the conformation of the bound R′ domain considerably altered by dilution. Therefore, in wild-type tau that contains both the pseudorepeat R′ and all four

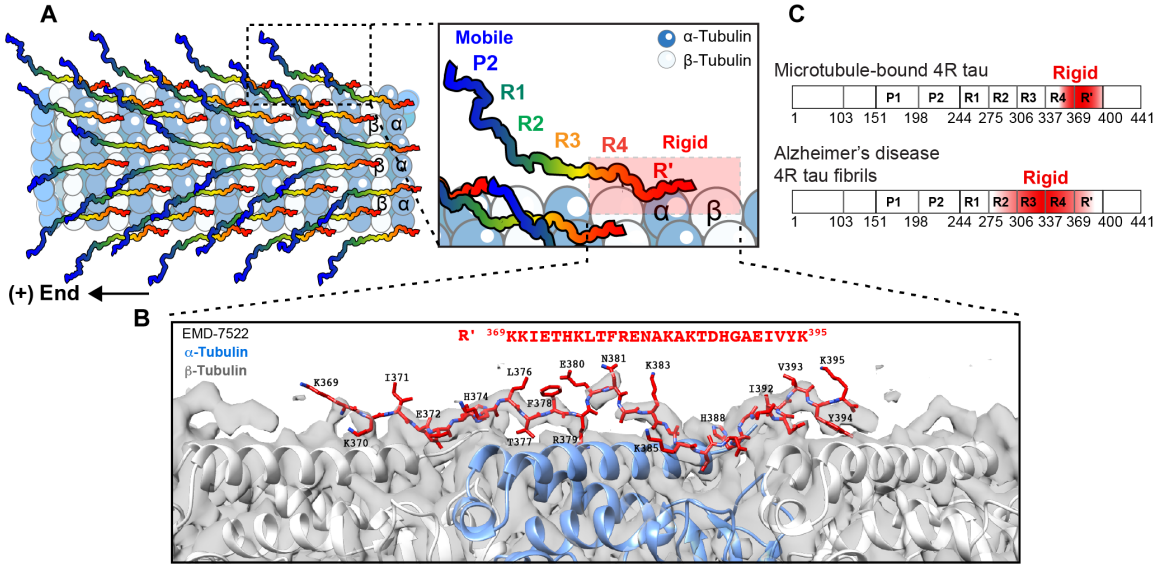

Fig. 5. R′ is the MT-binding core of tau. (**A**) Model of the MT-binding mode of tau. From P2 to R′, tau becomes progressively immobilized. P2 is the most mobile segment (blue), whereas R4-R′ (red) are the most rigid segments. The schematic illustrates only half of the tubulin dimers with a bound tau protein (1:0.5), but this binding mode also applies to the 1:1 complex, in which every tubulin dimer is associated with a tau protein via the R′ domain. The schematic depicts tau's dynamic N-terminal region to point to the (+) end of the MT, to be consistent with the cryo-EM data (*14*). (**B**) Structural model of R′(369 to 395) (red) fitted into the low-resolution cryo-EM map (gray surface) of wild-type full-length tau (EMD-7522). (**C**) The different rigid cores of 0N4R tau in two supramolecular assemblies: bound to MTs versus in Alzheimer's disease neurofibrillary tangles (*55*).

repeats, R′ outcompetes the other repeats for association with MTs. These result differ qualitatively from the current paradigm that all repeats in tau bind MTs similarly (*14*) and that each tau associates with two to five tubulin dimers (*4*, *9*, *27*).

The preferential immobilization of R′ by MTs observed in the current NMR spectra is in good agreement with a number of biophysical measurements of tau diffusion on MTs. For example, the diffusion constants of various tau deletion constructs in living neurons have been measured and compared using fluorescence decay after photoactivation (*28*). The data showed that the four regular repeats had only a modest influence on the MT binding affinity, whereas the R′ domain greatly enhanced MT binding by decreasing the dissociation rate of tau by sixfold. R′ deletion caused higher diffusion constants, whereas C terminus deletion caused lower diffusion constants. Similarly, fluorescence correlation spectroscopy experiments have been conducted on tau constructs that begin with the P2 domain and contain varying numbers and order of the repeats (*29*). These data showed that the presence of R′ slowed tau diffusion on unpolymerized MTs and increased the heterogeneity of the tau-tubulin coassembly compared to constructs without R′. Moreover, longer diffusion times correlate with higher polymerization rates of the MT, providing evidence that R′ binding is important for MT assembly. Last, binding assays of various tau constructs showed that the R1 to R4 repeats bind 10-fold more weakly in the absence of the flanking P2 and R′ domains [dissociation constant (K_d) ~25 to 50 μM] than in their presence (K_d ~1 to 3 μM) (*9*, *30*). These biochemical data are in good agreement with the current results that the MT-immobilized residues are located in the R′ domain and the C-terminal portion of the R4 domain in taxol-stabilized samples. Moreover, the well-resolved solid-state NMR spectra for the immobilized residues imply that R′ directly acts as the rigid anchor onto the MTs, instead of serving as "jaws" (*31*, *32*) that target other repeats to the MT surface.

Among the sequentially assigned MT-immobilized residues in the 1:1 complex, we attribute the HVPGGG motif to the R4 domain while ruling out the HVPGGG motif in the R2 domain. This is based on the high mobility of the N-terminal portion of the protein and the continuous electron densities of tau in the cryo-EM data (*14*). The longest continuous segment of tau in the electron density map, seen in the R2 × 4 chimeric tau, contained 27 residues. No other densities were found on the surface or in the lumen of MTs. Because the NMR spectra indicate that the binding stoichiometry is one tau to one tubulin dimer, each tubulin dimer should bind a continuous segment of about 27 residues. An alternative model where both R2 and R4-R′ contribute immobilized residues would entail multiple discontinuous segments in the intrinsically disordered tau to form rigid anchors on the MT, with a ~40-residue disordered loop between the end of the R2 HVPGGG motif and the beginning of the R4 IGSLD motif. Moreover, these two rigid anchors would have to lie close in space to satisfy the continuous electron densities and adopt well-ordered conformations to satisfy the narrow NMR linewidths. Such a model is energetically unlikely. The continuous nature of MT-bound tau residues is consistent with an increasing number of cryo-EM structures of other MT-associated proteins. These include the pierce1 and pierce2 proteins in dynein-decorated doublet MTs that function in cilia motility (*33*) and the SPM1 protein on the inner wall of the cortical MTs in the human parasite *Toxoplasma gondii* (*34*). All these proteins show a continuous segment anchored on the MTs, suggesting that the continuity of the bound domain might be a general feature of protein interactions with MTs.

While the current dipolar NMR spectra can be sequentially assigned to R′ and R4 residues, the most mobile residues detected in the ^{13}C-^{1}H INEPT spectra are enriched in the Pro-rich domain and the R1 domain of P2R tau. Residue-type analysis of these INEPT spectra shows that the P2 domain, which contain most of the S(P) residues and all T(P) residues in the protein, and the N terminus of the R1 domain, which contains the only A(P) and Met residues in the protein, are highly mobile. If we assume that these mobile residues result from a contiguous segment, then the relative intensities of the INEPT signals best match a 56-residue segment (Ser^{198}-Leu^{253}) that spans P2 and the first 10 residues of R1 (Fig. 2D and table S2). Some residues such as Ile from other regions of the protein also exhibit methyl signals in the INEPT spectra, indicating local segmental mobilities outside this N-terminal portion of the protein.

Our observation that the N terminus of R1 is mobile is in good agreement with the 3.2 Å cryo-EM map (EMD-7769) of a chimeric tau that contains four R1 repeats. Those data indicate that the MT-bound segment skips the N-terminal 12 residues of R1 but spans the next 12 residues from Val^{256} to Lys^{267} (Fig. 3D and fig. S11A). Thus, both the INEPT spectra of wild-type tau and the cryo-EM data of chimeric tau indicate that the N-terminal portion of R1, which is highly polar, is dynamically disordered and does not interact strongly with MTs. The polar N terminus of R1 has low sequence homology with the N terminus of R2 and R3 (Fig. 2, D and E), which contain an amyloidogenic hexapeptide motif (*35*). This suggests that in the R2 × 4 chimera where the Pro-rich P2 domain is followed by the hexapeptide-containing R2 instead of the polar N terminus of R1, the energetic balance in MT association would be altered compared to wild-type tau.

Why is R′, instead of one of the other four repeats, the ordered core that interacts with MTs? We hypothesize that the larger fraction of charged residues in R′-R4 is responsible for this high affinity to MTs. The conserved R′ has seven basic Lys/Arg residues and four acidic Asp/Glu residues, while R4 contains five each of basic and acidic residues. These two domains together are nearly twofold more charged than the other repeats, thus representing a distinct group in nearest-neighbor cluster analysis of the amino acid sequence (*28*). The fact that the R′ domain outcompetes the other four domains in binding MTs when all five repeats are present as in wild-type tau does not necessarily mean that the R1 to R4 repeats cannot associate with MTs with moderate affinity. The previous cryo-EM and Rosetta derived structural models of the 27-residue bound segment in the R2 × 4 chimera and the 12-residue bound segment in the R1 × 4 chimera suggest that the affinity of R′ for the MTs may not be substantially higher than that of the R1 to R4 repeats. Cooperative interactions of identical repeats in synthetic constructs could then change the energetic balance of MT association.

The central role of R′ in anchoring tau onto MTs has implications for the treatment of tauopathies. R′ contains many disease-relevant posttranslational modifications such as T386 and S396 phosphorylation, K369 and K385 ubiquitination, and Lys acetylation (*36*). Therefore, preventing posttranslational modifications in this domain to maintain tau binding to MTs can be a potential therapeutic approach. It is known that R3 and R4 constitute most of the rigid β sheet cores of tau fibrils in brains of Alzheimer's disease and other tauopathies (Fig. 5C) (*37*–*39*). Therefore, the central role of R′ in binding MTs suggests that chemical strategies to stabilize this domain's interaction with MTs might be useful for retaining tau function and preventing its aggregation into the β sheet fibrils found in neurodegenerative diseases.

MATERIALS AND METHODS

Expression of isotopically labeled P2R and 0N4R tau constructs

The gene encoding P2R tau (residues 198 to 399) contains a Tobacco Etch Virus (TEV) cleavage site and a His_6 tag at the N terminus. This gene was cloned into a pET-28a vector and transfected into *Escherichia coli* BL21(DE3) competent cells (New England Biolabs). A starter culture was grown in 50 ml of LB medium containing kanamycin (50 μg/ml). After overnight growth at 37°C with 220 rpm shaking, 50 ml of overnight culture was used to inoculate 1 liter of LB medium containing kanamycin (50 μg/ml). Cells were grown at 37°C and 220 rpm until an optical density at 600 nm reached 1.0. Then, cells were spun down at 1000*g* and 4°C for 20 min, and the cell pellet was resuspended in 1 liter of minimal media containing M9 salts (1×), $^{15}NH_4Cl$ (1 g/liter), ^{13}C glucose (2 g/liter), 1 mM $MgSO_4$, 0.1 mM $CaCl_2$, kanamycin (50 mg/ml), and vitamin/mineral supplements. Cells were grown in this minimal medium at 37°C and 220 rpm for 2 hours, then protein expression was induced with 1 mM isopropyl-β-D-thiogalactopyranoside (IPTG), and an additional 1 g of ^{13}C glucose was added. Expression lasted 18 hours at 30°C with 180 rpm shaking. Expression of 0N4R tau was induced with 0.5 mM IPTG and lasted 5 hours at 37°C with 180 rpm shaking.

Purification of recombinant P2R tau and 0N4R tau

P2R tau was purified from the soluble fraction of cells using Ni^{2+} affinity column chromatography and reverse-phase high-performance liquid chromatography (HPLC). Cells were spun down at 6000*g* and 4°C for 15 min, and the pellet was resuspended in 40 ml of a lysis buffer containing 1× phosphate-buffered saline (PBS) (pH 7.4), 2 mM dithiothreitol (DTT), 0.05 mM phenylmethylsulfonyl fluoride (PMSF), and one tablet cOmplete protease inhibitor cocktail (Roche). Cells were lysed by sonication on ice (5 s on and 5 s off for 10 min; 550 Sonic Dismembrator, Fisher Scientific). The cell lysate was boiled for 10 min and spun at 20,000*g* for 60 min to remove cell debris and protein aggregates. Solubilized proteins were loaded on 5 ml of Profinity immobilized metal affinity chromatography (IMAC) resin charged with Ni^{2+} (Bio-Rad, CA, USA) that was previously washed with the binding buffer [1× PBS, 2 mM DTT, and 20 mM imidazole (pH 8)]. The resin was washed with 20 column volumes of binding buffer before proteins were eluted from the column with five column volumes of elution buffer [1× PBS, 2 mM DTT, and 400 mM imidazole (pH 8)]. The eluted fraction was loaded onto a desalting column (Econo-Pac 10DG, Bio-Rad, CA, USA) to exchange buffer for the TEV cleavage buffer [50 mM tris, 150 mM NaCl, 2 mM DTT, 0.05 mM EDTA, and 0.05 mM PMSF (pH 8)]. TEV protease was added at a ratio of ~3:100 (w/w) with respect to the protein after the protein was diluted to ~0.5 mg/ml to prevent aggregation. The cleavage reaction proceeded at 4°C for 16 hours with gentle rocking. After cleavage, 2 M guanidinium chloride was added, and the solution was loaded onto 5 ml of $Ni^{2+/-}$charged resin that was previously washed with the binding buffer. The flow-through was collected and purified on a reverse-phase HPLC with a semipreparative column (250 mm in length, 21.2 mm inner diameter, C3, 7-μm particle size, 300 Å pore size; Higgins Analytical) using an acetonitrile gradient of 5 to 95% in 35 min. HPLC fractions that were >95% pure as determined by SDS–polyacrylamide gel electrophoresis with Coomassie blue staining were pooled and lyophilized to give powdered P2R tau. The yield of the purification was ~15 mg of protein per liter of M9 culture. 0N4R tau was purified using a similar method as described previously (*20*).

Tubulin extraction and purification

Tubulin was extracted from porcine brains and purified by repeated heat polymerization and cold depolymerization cycles, as described previously (*40*). In brief, fresh porcine brains were purchased from a local slaughterhouse and transported in ice-cold PBS [20 mM Na-phosphate and 150 mM NaCl (pH 7.2)]. Brains were rapidly cleaned of viscera and then homogenized in cold (4°C) depolymerization buffer [50 mM 2-(N-morpholino)ethanesulfonic acid (MES) buffer and 1 mM $CaCl_2$ (pH 6.6)] using a blender. The homogenate was spun down for 60 min at 4°C and 20,000*g*. The supernatant was supplemented with an equal volume of warm (37°C) high-molarity Pipes buffer (1 M Pipes, 10 mM MgCl, and 20 mM EGTA, titrated to pH 6.9 with KOH), 1.5 mM adenosine 5′-triphosphate, and 0.5 mM GTP. An equal volume (one-third of the final volume) of warm glycerol was added to the solution, and then the mixture was incubated at 37°C for 60 min. The polymerized tubulin was ultracentrifuged at 151,000*g* for 30 min at 37°C. The pellet was resuspended in 100 ml of cold depolymerization buffer, and the mixture was left on ice for 30 min. The solution was ultracentrifuged again at 4°C for 30 min at 70,000*g*. Using the supernatant, an additional polymerization step was performed as above and ultracentrifuged. This time, the pellet was resuspended in 15 ml of BRB80 buffer (80 mM K-Pipes, 1 mM MgCl, and 1 mM GTP, titrated to pH 6.8 with KOH) and incubated on ice for 15 min. The mixture was then ultracentrifuged to clarify the solution for 15 min at 4°C at 300,000*g*. The final tubulin solution was immediately flash-frozen in liquid nitrogen. The concentration of tubulin was assessed using absorbance at 280 nm with an extinction coefficient of 115,000 M^{-1} cm^{-1}. The uncertainty in the concentration measurement is estimated to be less than 5% and account for very small amounts of other proteins remaining in the final product.

MT polymerization and preparation of solid-state NMR samples

The required number of tubulin aliquots was rapidly defrosted (usually four tubes at ~5 mg/ml, or ~50 μM, ~20 mg in total), and the tubes were centrifuged at 16,000*g* for 5 min at room temperature to remove any aggregates. The tubulin solution was left on ice for 10 min before adding 1 mM GTP and 2 mM DTT. The sample was mixed by gentle inversion before being incubated on ice for 10 min and was then transferred to a heat block at 37°C for 1 hour and with gentle mixing every 15 min. This solution was incubated for another 30 min, during which 1, 10, and 30 μl of 1 mM taxol solution was added 10 min apart to reach equimolar concentration with respect to tubulin. Natural abundance or ^{13}C, ^{15}N-labeled P2R tau powder was dissolved in BRB80 buffer containing 2 mM DTT to reach a concentration of 1 mg/ml (~47 μM). The P2R tau amount was measured gravimetrically, because the protein has a small extinction coefficient of 2980 M^{-1} cm^{-1} due to the lack of Trp residues and the small number of other aromatic residues, which makes A_{280} measurements unreliable. The mass measurement is estimated to have an uncertainty of 15%. The MT and P2R tau solutions were mixed at the desired molar ratios of 1:1 or 1:0.5. These molar ratios have a propagated fractional uncertainty of 15%. The final concentration of MTs was 10 μM for all samples, while the tau concentration was diluted to 5 or 10 μM. The solutions were then incubated for 1 hour at room temperature without shaking but with gentle inversion every 15 min to facilitate mixing. The tau-MT mixture was collected by ultracentrifugation at 200,000*g* for 30 min and 28°C. For the NMR samples, pellets from multiple tubes were pooled by

resuspending in BRB80 buffer containing 1 mM DTT and 20 μM taxol, followed by another ultracentrifugation step.

To prepare tubulin-tau coassembled samples, we diluted freshly defrosted tubulin to 10 μM and placed it on ice for 10 min before adding 1 mM GTP and 2 mM DTT. The mixture was gently inverted and then incubated for 10 min on ice, after which we added an equal volume of 20 μM P2R tau in BRB80 buffer containing 2 mM DTT. The solution was gently inverted, and then the tube was transferred to a heat block at 37°C for 1 hour without shaking but with gentle inversion every 15 min. The tubulin-tau coassembly was collected by ultracentrifugation at 200,000*g* for 30 min at 28°C. Consecutive ultracentrifugation of the solution fractions was performed to avoid resuspending the pellets, which may cause partial dissociation of these dynamically unstable MTs.

The tau-MT pellets were packed into 3.2-mm Revolution NMR pencil rotors and kept below 10°C during most NMR experiments. The samples typically consisted of ~20 mg of MTs and 2 or 4 mg of P2R tau or 7 mg of 0N4R tau. The total hydrated mass was ~40 mg. Negative-stain transmission electron microscopy (TEM) was used to assess the morphology of the samples (Fig. 1C and fig. S1). The complex was found by TEM to be stable at 4°C for at least 2 weeks. Therefore, the sample temperature for all solid-state NMR experiments was set to 2° to 8°C.

Transmission electron microscopy

Samples were adsorbed onto freshly glow-discharged, 200-mesh formvar/carbon-coated copper grids (Ted Pella), washed with water, and stained with 0.7% (w/v) uranyl formate for 15 to 20 s. TEM images were taken on an FEI Tecnai T12 electron microscope.

Solid-state NMR measurements and analysis

All solid-state NMR spectra were measured on Bruker Avance 800-MHz (18.8-T) spectrometer at the Francis Bitter Magnet Laboratory using a Black Fox 3.2-mm HCN MAS probe. Reported sample temperatures were estimated using the water ^{1}H chemical shift calibrated using dextran sulfate sodium (*41*). ^{13}C chemical shifts were referenced externally to the adamantane CH_2 chemical shift at 38.48 ppm on the tetramethylsilane scale. ^{15}N chemical shifts were referenced to the ^{15}N peak of *N*-acetylvaline at 122.00 ppm on the liquid ammonia scale. More detailed experimental parameters are given in table S4.

Most 2D dipolar ^{15}N-^{13}C correlation spectra involve SPECIFIC cross-polarization (CP) (*42*) for ^{15}N-^{13}C polarization transfer. The Black Fox crossed-coil dual-resonator low-E coil (*43*) has higher radio frequency (rf) field homogeneity than solenoid coils and hence gives fourfold higher ^{15}N-^{13}C SPECIFIC-CP efficiencies compared to Bruker HCN probes. The spectra were measured at MAS frequencies of 10.5 or 14 kHz. Typical rf field strengths were 70 to 90 kHz for ^{1}H, 30 to 50 kHz for ^{13}C, and 25 to 40 kHz for ^{15}N. Combined-driven (CORD) spin diffusion (*44*) was used for ^{13}C mixing. CO-to-Cα polarization transfer in the N(CO)CA experiment was carried out using a modified BSH-CP sequence (*21*, *45*), in which the ^{13}C rf carrier frequency was placed at ~95 ppm, away from both Cα and CO peaks, to obtain high-efficiency double-quantum polarization transfer.

1D and 2D INEPT ^{1}H-^{13}C spectra were measured to detect the signals of dynamic residues. For ^{1}H-^{13}C CP, the contact time was either 70 or 800 μs, which selectively detect either highly rigid residues or both rigid and semirigid residues. For all 2D spectra, multiple 1-day blocks were recorded and added in the time domain before Fourier transformation. Spectra were either processed using QSINE apodization [shifted sine bell (SSB) = 3] to improve resolution or gaussian multiplication (GM) apodization (LB = −20 Hz and GB = 0.05) to improve sensitivity. The NMR spectra were processed in the TopSpin software, and chemical shift assignment was conducted using the Collaborative Computational Project for NMR (CCPNMR) software (*46*). The assigned chemical shifts were converted to secondary chemical shifts to predict (ϕ and ψ) torsion angles using the TALOS-N software (*47*).

Water-edited 1D ^{13}C experiments started with a water-selective echo consisting of one rotor period before and after a 180° Gaussian pulse that lasted 10 rotor periods. The selected water magnetization was transferred to the protein protons by spin diffusion and chemical exchange (*48*, *49*) and then cross-polarized to protein ^{13}C sites for detection. When the ^{1}H mixing time was 0 ms, no ^{13}C CP signal was detected, confirming that the protein ^{1}H magnetization was filtered out by the water-selective echo. When a mixing time of 100 ms was used, the ^{13}C spectra displayed the same pattern as the unedited ^{13}C CP spectra, but with half the intensity, indicating that water and protein proton magnetization is equilibrated by 100 ms. This 100-ms spectrum served as the control (S_0) spectrum for intensity normalization. The hydration values S/S_0 were calculated by integrating the 71 to 46 ppm region for the protein backbone Cα signals. Error bars were propagated from the signal-to-noise ratios of the 1D spectra.

The 2D ^{1}H-^{13}C dipolar-chemical-shift (DIPSHIFT) correlation experiment was performed at 10.5-kHz MAS at a sample temperature of ~5°C (*50*). After-70 μs ^{1}H-^{13}C CP to select the most rigid residues, the ^{13}C magnetization was dephased by ^{1}H-^{13}C dipolar coupling during a doubled DIPSHIFT period (*51*). ^{1}H-^{1}H homonuclear decoupling was achieved using the Frequency Switched Lee–Goldburg (FSLG) sequence, whose theoretical scaling factor is 0.577 (*52*). The measured ^{13}C intensities at various dephasing times were integrated from 63 to 50 ppm and normalized to the intensity of the first time point. These intensities ratios were compared with simulated doubled DIPSHIFT curves to determine the dipolar order parameter, S_{CH} (Fig. 4). The simulations used a rigid-limit FSLG-scaled C-H dipolar coupling of 26.34 kHz.

To analyze the intensities of the 2D INEPT spectra, we first corrected the absolute intensities of each peak for the theoretical efficiencies in INEPT magnetization transfer for CH, CH_2, and CH_3 groups. The INEPT transfer efficiency for CH_3 groups is three-fourths of that of CH/CH_2 groups. Additional details are given in tables S2. To identify the dynamic segment in the 1:1 MT:P2R tau complex, we compared all integrated intensities to the A(P) Cβ intensity. The intensity ratios were then compared to the number of residues in the primary sequence.

Resonance assignment of the immobilized segments of MT-bound tau

To identify the rigid core of MT-bound tau, we assigned the 2D CC and NC dipolar correlation spectra by combining residue-type assignment and sequential assignment (table S3). For the two P2R tau samples, the 50-ms 2D CC spectra were first analyzed to identify the amino acid types of all rigid and semirigid residues. The aliphatic Cα, Cβ, and other side-chain chemical shifts are diagnostic of the residue type, while the backbone CO and Cα chemical shifts are used in conjunction with the 2D NCA and NCO spectra for sequential assignment. For the MT-bound P2R tau sample (1:1), these three spectra together allowed us to sequentially assign 19 residues, among

which five residues are ambiguous due to partial resonance overlap (fig. S4). Some peaks in the 2D NCα spectrum are not assigned, because the low sensitivity of these MT-tau mixtures prohibits the measurement of 3D correlation spectra that are required for complete sequential assignment. The presence of these additional well-resolved peaks supports the conclusion that the full R′ domain is rigidified by MT binding. For MT-bound 0N4R tau (1:1), we measured 2D NCA, N(CO)CA, and N(CA)CB spectra (fig. S6). The N(CO)CA spectrum connects the backbone ^{15}N chemical shift of residue *i* with the ^{13}Cα chemical shift of the preceding residue *i* − 1, while the N(CA)CB spectrum provides side-chain Cβ chemical shifts to facilitate amino acid–type assignment. For the tubulin-P2R tau (1:2) co-assembled sample, spectral sensitivity and resolution were limited by considerable protein dynamics. Thus, we only conducted residue-type assignment by connecting the ^{13}C chemical shifts in the 2D CC spectrum (Fig. 3B) with the Cα signals in the 2D NCA spectrum (Fig. 3A).

Structure modeling of MT-bound R′

We produced a homology structure model of MT-bound R′ by using Rosetta to fit the best R′ segment into previously reported cryo-EM maps of MT-bound tau (*14*). The Rosetta suite (*25*) was accessed on the NMRbox server (*53*). We first fit the NMR-assigned MT-interacting R′ residues into the cryo-EM map of a synthetic tau construct that encompasses P2, four replicated R2 domains, and R′ (EMD-7771) (figs. S10 and S11). Starting from the previous model of an R2 (274 to 300) peptide (Protein Data Bank ID: 6cvn) bound to two β-tubulins and one α-tubulin, we used a RosettaCM protocol (*14*) to model R′ into the cryo-EM map. RosettaCM fits a molecular model into a low-resolution cryo-EM map via fragment insertion (*53*). We generated seven possible sequence threadings of R′ (fig. S10A) using a python protocol in the Rosetta suite. A custom XML script allowed 9- and 3-mer fragment insertions within the 27 residues, while the tubulin monomers were only allowed to move via minimization (i.e., no fragment insertion for tubulin). A total of 100 models were calculated for each of the seven sequence registers, requiring computation time of about a week. The five lowest energy models from each sequence register were selected for further analysis. The Rosetta energy scores were normalized to the tubulin-only structural model. PRODIGY for protein-protein complexes (*26*, *54*) was used to predict the binding affinities at 25°C between each 27-residue tau constructs and the three tubulin monomers within the models (fig. S10, C to E). The best-fit model corresponds to residues 369 to 395, denoted as R′-3 (fig. S11C). This model was then inserted into the low-resolution cryo-EM map of full-length 2N4R tau (EMD-7522) using the "Fit in Map" function of the Chimera software.

SUPPLEMENTARY MATERIALS

Supplementary material for this article is available at https://science.org/doi/10.1126/sciadv.abo4459

View/request a protocol for this paper from *Bio-protocol*.

REFERENCES AND NOTES

1. G. M. Alushin, G. C. Lander, E. H. Kellogg, R. Zhang, D. Baker, E. Nogales, High-resolution microtubule structures reveal the structural transitions in αβ-tubulin upon GTP hydrolysis. *Cell* **157**, 1117–1129 (2014).
2. M. D. Weingarten, A. H. Lockwood, S. Y. Hwo, M. W. Kirschner, A protein factor essential for microtubule assembly. *Proc. Natl. Acad. Sci. U.S.A.* **72**, 1858–1862 (1975).
3. Y. Wang, E. Mandelkow, Tau in physiology and pathology. *Nat. Rev. Neurosci.* **17**, 5–21 (2016).
4. M. Hong, V. Zhukareva, V. Vogelsberg-Ragaglia, Z. Wszolek, L. Reed, B. I. Miller, D. H. Geschwind, T. D. Bird, D. McKeel, A. Goate, J. C. Morris, K. C. Wilhelmsen, G. D. Schellenberg, J. Q. Trojanowski, V. M. Lee, Mutation-specific functional impairments in distinct tau isoforms of hereditary FTDP-17. *Science* **282**, 1914–1917 (1998).
5. G. T. Bramblett, M. Goedert, R. Jakes, S. E. Merrick, J. Q. Trojanowski, V. M. Lee, Abnormal tau phosphorylation at Ser^{396} in Alzheimer's disease recapitulates development and contributes to reduced microtubule binding. *Neuron* **10**, 1089–1099 (1993).
6. E. M. Mandelkow, E. Mandelkow, Biochemistry and cell biology of tau protein in neurofibrillary degeneration. *Cold Spring Harb. Perspect. Med.* **2**, a006247 (2012).
7. M. Goedert, R. Jakes, M. G. Spillantini, M. Hasegawa, M. J. Smith, R. A. Crowther, Assembly of microtubule-associated protein tau into Alzheimer-like filaments induced by sulphated glycosaminoglycans. *Nature* **383**, 550–553 (1996).
8. M. E. Orr, A. C. Sullivan, B. Frost, A brief overview of tauopathy: Causes, consequences, and therapeutic strategies. *Trends Pharmacol. Sci.* **38**, 637–648 (2017).
9. N. Gustke, B. Trinczek, J. Biernat, E. M. Mandelkow, E. Mandelkow, Domains of tau protein and interactions with microtubules. *Biochemistry* **33**, 9511–9522 (1994).
10. H. Kadavath, R. V. Hofele, J. Biernat, S. Kumar, K. Tepper, H. Urlaub, E. Mandelkow, M. Zweckstetter, Tau stabilizes microtubules by binding at the interface between tubulin heterodimers. *Proc. Natl. Acad. Sci. U.S.A.* **112**, 7501–7506 (2015).
11. B. Gigant, I. Landrieu, C. Fauquant, P. Barbier, I. Huvent, J. M. Wieruszeski, M. Knossow, G. Lippens, Mechanism of tau-promoted microtubule assembly as probed by NMR spectroscopy. *J. Am. Chem. Soc.* **136**, 12615–12623 (2014).
12. K. M. McKibben, E. Rhoades, Independent tubulin binding and polymerization by the proline-rich region of tau is regulated by tau's N-terminal domain. *J. Biol. Chem.* **294**, 19381–19394 (2019).
13. J. Al-Bassam, R. S. Ozer, D. Safer, S. Halpain, R. A. Milligan, MAP2 and tau bind longitudinally along the outer ridges of microtubule protofilaments. *J. Cell Biol.* **157**, 1187–1196 (2002).
14. E. H. Kellogg, N. M. A. Hejab, S. Poepsel, K. H. Downing, F. DiMaio, E. Nogales, Near-atomic model of microtubule-tau interactions. *Science* **360**, 1242–1246 (2018).
15. B. Reif, S. E. Ashbrook, L. Emsley, M. Hong, Solid-state NMR spectroscopy. *Nat. Rev. Methods Primers* **1**, 2 (2021).
16. Y. Luo, S. Xiang, P. J. Hooikaas, L. van Bezouwen, A. S. Jijumon, C. Janke, F. Forster, A. Akhmanova, M. Baldus, Direct observation of dynamic protein interactions involving human microtubules using solid-state NMR spectroscopy. *Nat. Commun.* **11**, 18 (2020).
17. S. Yan, H. Zhang, G. Hou, S. Ahmed, J. C. Williams, T. Polenova, Internal dynamics of dynactin CAP-Gly is regulated by microtubules and plus end tracking protein EB1. *J. Biol. Chem.* **290**, 1607–1622 (2015).
18. D. L. Gard, M. W. Kirschner, Microtubule assembly in cytoplasmic extracts of *Xenopus oocytes* and eggs. *J. Cell Biol.* **105**, 2191–2201 (1987).
19. A. J. Dregni, P. Duan, M. Hong, Hydration and dynamics of full-length tau amyloid fibrils investigated by solid-state nuclear magnetic resonance. *Biochemistry* **59**, 2237–2248 (2020).
20. A. J. Dregni, V. S. Mandala, H. Wu, M. R. Elkins, H. K. Wang, I. Hung, W. F. DeGrado, M. Hong, In vitro 0N4R tau fibrils contain a monomorphic β-sheet core enclosed by dynamically heterogeneous fuzzy coat segments. *Proc. Natl. Acad. Sci. U.S.A.* **116**, 16357–16366 (2019).
21. A. J. Dregni, H. K. Wang, H. Wu, P. Duan, J. Jin, W. F. DeGrado, M. Hong, Inclusion of the C-terminal domain in the β-sheet core of heparin-fibrillized three-repeat tau protein revealed by solid-state nuclear magnetic resonance spectroscopy. *J. Am. Chem. Soc.* **143**, 7839–7851 (2021).
22. S. W. Manka, C. A. Moores, Microtubule structure by cryo-EM: Snapshots of dynamic instability. *Essays Biochem.* **62**, 737–751 (2018).
23. H. Kadavath, Y. Cabrales Fontela, M. Jaremko, L. Jaremko, K. Overkamp, J. Biernat, E. Mandelkow, M. Zweckstetter, The binding mode of a tau peptide with tubulin. *Angew. Chem. Int. Ed. Engl.* **57**, 3246–3250 (2018).
24. E. Nogales, S. G. Wolf, K. H. Downing, Structure of the alpha beta tubulin dimer by electron crystallography. *Nature* **391**, 199–203 (1998).
25. S. J. Fleishman, A. Leaver-Fay, J. E. Corn, E. M. Strauch, S. D. Khare, N. Koga, J. Ashworth, P. Murphy, F. Richter, G. Lemmon, J. Meiler, D. Baker, RosettaScripts: A scripting language interface to the Rosetta macromolecular modeling suite. *PLOS ONE* **6**, e20161 (2011).
26. L. C. Xue, J. P. Rodrigues, P. L. Kastritis, A. M. Bonvin, A. Vangone, PRODIGY: A web server for predicting the binding affinity of protein-protein complexes. *Bioinformatics* **32**, 3676–3678 (2016).
27. N. Hirokawa, Y. Shiomura, S. Okabe, Tau proteins: The molecular structure and mode of binding on microtubules. *J. Cell Biol.* **107**, 1449–1459 (1988).
28. B. Niewidok, M. Igaev, F. Sundermann, D. Janning, L. Bakota, R. Brandt, Presence of a carboxy-terminal pseudorepeat and disease-like pseudohyperphosphorylation critically influence tau's interaction with microtubules in axon-like processes. *Mol. Biol. Cell* **27**, 3537–3549 (2016).
29. X. H. Li, E. Rhoades, Heterogeneous tau-tubulin complexes accelerate microtubule polymerization. *Biophys. J.* **112**, 2567–2574 (2017).
30. E. M. Mandelkow, J. Biernat, G. Drewes, N. Gustke, B. Trinczek, E. Mandelkow, Tau domains, phosphorylation, and interactions with microtubules. *Neurobiol. Aging* **16**, 355–362 (1995).

31. U. Preuss, J. Biernat, E. M. Mandelkow, E. Mandelkow, The "jaws" model of tau-microtubule interaction examined in CHO cells. *J. Cell Sci.* **110** (Pt. 6), 789–800 (1997).
32. M. D. Mukrasch, M. von Bergen, J. Biernat, D. Fischer, C. Griesinger, E. Mandelkow, M. Zweckstetter, The "jaws" of the tau-microtubule interaction. *J. Biol. Chem.* **282**, 12230–12239 (2007).
33. M. Gui, H. Farley, P. Anujan, J. R. Anderson, D. W. Maxwell, J. B. Whitchurch, J. J. Botsch, T. Qiu, S. Meleppattu, S. K. Singh, Q. Zhang, J. Thompson, J. S. Lucas, C. D. Bingle, D. P. Norris, S. Roy, A. Brown, De novo identification of mammalian ciliary motility proteins using cryo-EM. *Cell* **184**, 5791–5806.e19 (2021).
34. X. Wang, Y. Fu, W. L. Beatty, M. Ma, A. Brown, L. D. Sibley, R. Zhang, Cryo-EM structure of cortical microtubules from human parasite *Toxoplasma gondii* identifies their microtubule inner proteins. *Nat. Commun.* **12**, 3065 (2021).
35. M. R. Sawaya, S. Sambashivan, R. Nelson, M. I. Ivanova, S. A. Sievers, M. I. Apostol, M. J. Thompson, M. Balbirnie, J. J. Wiltzius, H. T. McFarlane, A. Ø. Madsen, C. Riekel, D. Eisenberg, Atomic structures of amyloid cross-beta spines reveal varied steric zippers. *Nature* **447**, 453–457 (2007).
36. H. Wesseling, W. Mair, M. Kumar, C. N. Schlaffner, S. Tang, P. Beerepoot, B. Fatou, A. J. Guise, L. Cheng, S. Takeda, J. Muntel, M. S. Rotunno, S. Dujardin, P. Davies, K. S. Kosik, B. L. Miller, S. Berretta, J. C. Hedreen, L. T. Grinberg, W. W. Seeley, B. T. Hyman, H. Steen, J. A. Steen, Tau PTM profiles identify patient heterogeneity and stages of Alzheimer's disease. *Cell* **183**, 1699–1713.e13 (2020).
37. B. Falcon, J. Zivanov, W. Zhang, A. G. Murzin, H. J. Garringer, R. Vidal, R. A. Crowther, K. L. Newell, B. Ghetti, M. Goedert, S. H. W. Scheres, Novel tau filament fold in chronic traumatic encephalopathy encloses hydrophobic molecules. *Nature* **568**, 420–423 (2019).
38. A. W. P. Fitzpatrick, B. Falcon, S. He, A. G. Murzin, G. Murshudov, H. J. Garringer, R. A. Crowther, B. Ghetti, M. Goedert, S. H. W. Scheres, Cryo-EM structures of tau filaments from Alzheimer's disease. *Nature* **547**, 185–190 (2017).
39. W. Zhang, A. Tarutani, K. L. Newell, A. G. Murzin, T. Matsubara, B. Falcon, R. Vidal, H. J. Garringer, Y. Shi, T. Ikeuchi, S. Murayama, B. Ghetti, M. Hasegawa, M. Goedert, S. H. W. Scheres, Novel tau filament fold in corticobasal degeneration. *Nature* **580**, 283–287 (2020).
40. M. Castoldi, A. V. Popov, Purification of brain tubulin through two cycles of polymerization-depolymerization in a high-molarity buffer. *Protein Expr. Purif.* **32**, 83–88 (2003).
41. A. Böckmann, C. Gardiennet, R. Verel, A. Hunkeler, A. Loquet, G. Pintacuda, L. Emsley, B. H. Meier, A. Lesage, Characterization of different water pools in solid-state NMR protein samples. *J. Biomol. NMR* **45**, 319–327 (2009).
42. M. Baldus, A. T. Petkova, J. Herzfeld, R. G. Griffin, Cross polarization in the tilted frame: Assignment and spectral simplification in heteronuclear spin systems. *Mol. Phys.* **95**, 1197–1207 (1998).
43. S. A. McNeill, P. L. Gor'kov, K. Shetty, W. W. Brey, J. R. Long, A low-E magic angle spinning probe for biological solid state NMR at 750 MHz. *J. Magn. Reson.* **197**, 135–144 (2009).
44. G. Hou, S. Yan, S. Sun, Y. Han, I. J. Byeon, J. Ahn, J. Concel, A. Samoson, A. M. Gronenborn, T. Polenova, Spin diffusion driven by R-symmetry sequences: Applications to homonuclear correlation spectroscopy in MAS NMR of biological and organic solids. *J. Am. Chem. Soc.* **133**, 3943–3953 (2011).
45. J. Hoffmann, J. Ruta, C. W. Shi, K. Hendriks, V. Chevelkov, W. T. Franks, H. Oschkinat, K. Giller, S. Becker, A. Lange, Protein resonance assignment by BSH-CP-based 3D solid-state NMR experiments: A practical guide. *Magn. Reson. Chem.* **58**, 445–465 (2020).
46. S. P. Skinner, R. H. Fogh, W. Boucher, T. J. Ragan, L. G. Mureddu, G. W. Vuister, CcpNmr AnalysisAssign: A flexible platform for integrated NMR analysis. *J. Biomol. NMR* **66**, 111–124 (2016).
47. Y. Shen, A. Bax, Protein backbone and sidechain torsion angles predicted from NMR chemical shifts using artificial neural networks. *J. Biomol. NMR* **56**, 227–241 (2013).
48. J. K. Williams, M. Hong, Probing membrane protein structure using water polarization transfer solid-state NMR. *J. Magn. Reson.* **247**, 118–127 (2014).
49. T. Wang, H. Jo, W. F. DeGrado, M. Hong, Water distribution, dynamics, and interactions with Alzheimer's β-amyloid fibrils investigated by solid-state NMR. *J. Am. Chem. Soc.* **139**, 6242–6252 (2017).
50. M. G. Munowitz, R. G. Griffin, G. Bodenhausen, T. H. Huang, Two-dimensional rotational spin-echo nuclear magnetic resonance in solids: Correlation of chemical shift and dipolar interactions. *J. Am. Chem. Soc.* **103**, 2529–2533 (1981).
51. M. Hong, J. D. Gross, C. M. Rienstra, R. G. Griffin, K. K. Kumashiro, K. Schmidt-Rohr, Coupling amplification in 2D MAS NMR and its application to torsion angle determination in peptides. *J. Magn. Reson.* **129**, 85–92 (1997).
52. A. Bielecki, A. C. Kolbert, M. H. Levitt, Frequency-switched pulse sequences: Homonuclear decoupling and dilute spin NMR in solids. *Chem. Phys. Lett.* **155**, 341–346 (1989).
53. M. W. Maciejewski, A. D. Schuyler, M. R. Gryk, I. I. Moraru, P. R. Romero, E. L. Ulrich, H. R. Eghbalnia, M. Livny, F. Delaglio, J. C. Hoch, NMRbox: A resource for biomolecular NMR computation. *Biophys. J.* **112**, 1529–1534 (2017).
54. A. Vangone, A. M. Bonvin, Contacts-based prediction of binding affinity in protein-protein complexes. *eLife* **4**, e07454 (2015).
55. Y. Shi, W. Zhang, Y. Yang, A. G. Murzin, B. Falcon, A. Kotecha, M. van Beers, A. Tarutani, F. Kametani, H. J. Garringer, R. Vidal, G. I. Hallinan, T. Lashley, Y. Saito, S. Murayama, M. Yoshida, H. Tanaka, A. Kakita, T. Ikeuchi, A. C. Robinson, D. M. A. Mann, G. G. Kovacs, T. Revesz, B. Ghetti, M. Hasegawa, M. Goedert, S. H. W. Scheres, Structure-based classification of tauopathies. *Nature* **598**, 359–363 (2021).
56. Y. Wang, O. Jardetzky, Probability-based protein secondary structure identification using combined NMR chemical-shift data. *Protein Sci.* **11**, 852–861 (2002).

Acknowledgments

Funding: This work is supported by NIH grant AG059661 to M.H. This study made use of NMR spectrometers at the MIT-Harvard Center for Magnetic Resonance, which is supported by NIH grant P41 GM132079. A.J.D. is supported by an NIH Ruth L. Kirschstein Individual National Research Service Award (F31AG069418). **Author contributions:** M.H., H.K.W., and A.J.D. conceptualized the project. N.E.M. carried out protein purification and MT assemblies, with help from P.D., H.K.W., and A.J.D. N.E.M., A.J.D., and P.D. carried out solid-state NMR measurements. N.E.M. and H.K.W. assigned the NMR spectra. All authors interpreted the findings. N.E.M. and M.H. wrote the paper with input from all authors. M.H. supervised the project. **Competing interests:** The authors declare that they have no competing interests. **Data and materials availability:** All data needed to evaluate the conclusions in the paper are present in the paper and/or the Supplementary Materials.

Submitted 3 February 2022
Accepted 7 June 2022
Published 20 July 2022
10.1126/sciadv.abo4459

Microtubule-binding core of the tau protein

Nadia El MammeriAurelio J. DregniPu DuanHarrison K. WangMei Hong

Sci. Adv., 8 (29), eabo4459. • DOI: 10.1126/sciadv.abo4459

Science Advances
AAAS

Supplementary Materials for

Microtubule-binding core of the tau protein

Nadia El Mammeri *et al.*

Corresponding author: Mei Hong, meihong@mit.edu

Sci. Adv. **8**, eabo4459 (2022)
DOI: 10.1126/sciadv.abo4459

This PDF file includes:

Table S1. Chemical shifts (^{13}C ppm / ^{1}H ppm) of highly mobile residues in the INEPT spectra of microtubule-bound P2R tau (1 : 1). Random coil chemical shift values (*56*) are shown in brackets below the measured chemical shifts for tau.

Residues	Cα/Hα	Cβ/Hβ	Cγ1/Hγ1	Cγ2/Hγ2	Cδ1/Hδ1	Cδ2/Hδ2	Cε1/Hε1
Thr		67.8 / 4.2 (67.8 / 4.2)		20.0 /1.2			
Thr(Pro)	61.6 / 4.7						
Ser		62.1 / 3.9 (61.9 / 3.9)					
Ser(Pro)		61.0 / 3.9 (61.9 / 3.9)					
Ala		17.7 / 1.4 (17.0 / 1.4)					
Ala(Pro)	51.6 / 4.7 (50.7 / 4.5)	16.4 / 1.4 (17.0 / 1.4)					
Pro			25.4 / 2.1		49.1 / 3.7		
Gly	43.8 / 3.9 (43.3 / 4.0)						
Arg					41.7 / 3.1		
Lys			23.2 / 1.5				40.3 / 3.0
Asn		37.5 / 2.8 (36.2 / 2.8)					
Glu			34.7 / 2.2				
Gln			32.1 / 2.4				
Leu		40.1 / 1.7 (39.9 / 1.6)			23.4 / 0.9 (22.7 / 1.6)	21.5 / 0.9 (22.1 / 0.7)	
Val			19.2 / 0.9				
Ile		36.6 / 1.8 (36.3 / 1.8)	25.6 / 1.2	16.0 / 0.8	11.5/0.8		
Met							15.3 / 2.1
His						118.4 / 7.1	135.6 / 8.2

Table S2. 2D INEPT intensity analysis of MT-bound P2R tau (1 : 1) and number of amino acid residues in different domains of P2R tau. The first two rows show the integrated intensities relative to the signals of A(P) Cβ and Met Cε. The last column gives the RMSD values between the residue numbers in each domain and the INEPT-detected number of flexible residues based on the Ala Cβ signal. The P2-R1 segment (residues 198-253) shows low RMSD, suggesting that this domain best encapsulates the most mobile residues in MT-bound P2R tau. The T(P) signal partially overlaps with a weak Pro Cα peak, thus its integrated intensity represents an upper bound.

Tau domains	A CB	A(P) CB	G CA	I CB	L CB	S CB	S(P) CB	K CG	R CD	Q CG	E CG	T CB	T(P) CB	M CE	RMSD
INEPT: A(P)Cβ	2.0	1.0	2.2	1.4	0.8	6.2	3.3	7.1	2.5	2.5	3.5	4.0	3.1	0.9	
INEPT: MCε	2.1	1.1	2.3	1.5	0.9	6.6	3.5	7.5	2.7	2.6	3.7	4.2	3.3	1.0	
P2(198-243)	2	0	4	0	2	7	3	4	5	0	1	5	4	0	1.8
R1(244-274)	0	1	4	1	2	2	0	5	0	2	1	2	0	1	2.2
R2(275-305)	0	0	4	3	2	4	0	5	0	2	0	0	0	0	2.4
R3(306-336)	0	0	5	2	2	3	0	4	0	2	0	1	0	0	2.5
R4(337-368)	0	0	4	2	2	3	0	4	1	1	2	1	0	0	2.2
R'(369-399)	3	0	1	1	1	0	1	6	1	0	3	3	0	0	2.2
P2-R1(198-253)	2	1	4	0	3	7	3	5	5	1	1	6	0	1	1.7

Table S3. ^{13}C and ^{15}N chemical shifts (ppm) of immobilized residues in microtubule-bound P2R tau measured from dipolar NMR spectra.

Residues	Cα	Cβ	C'	N	Cγ/γ1	Cγ2	Cδ/δ1	Cδ2	Cε/ ε1	Cε2/ ζ	Nδ
Sequentially assigned residues											
I354	59.1	37.3	173.7		16.0		22.6		11.8		
G355	45.2		174.7	111.6							
S356	56.4	61.6	172.3	114.5							
L357	53.6	40.1	173.2	123.5	27.1		22.7				
D358	51.8	38.4	176.5	118.9	178.2						
H362	55.9	28.2	172.3	122.3							
V363	56.2	31.7	171.2	129.3	18.3						
P364	60.6	30.5	175.6	137.5	25.7		48.7				
G365	41.3		171.9	112.4							
G366	42.5		173.4	104.1							
G367	44.3		173.1	105.8							
A382	51.0	17.0	176.3	124.9							
K383	54.3	33.8		121.6	23.9		27.5		39.8		
T386	59.3	66.9	172.8		19.9						
D387	52.2	39.05	176.7	123.9							
H388	57.8	25.6	173.2	118.4							
G389	43.8		173.1	105.1							
S396	54.6	61.1	170.8	123.4							
P397	60.3			135.2			48.3				
Thr1		66.5			20.0						
Thr2	62.3	69.0			19.4						
Type-assigned residues											
Asn/Asp1	48.9	37.1	174.9	117.9							
Asn/Asp2	50.8	37.0	175.7	122.1							
Asn/Asp3	51.3	37.3		123.4							
Asn/Asp4	50.4	37.2	127.3								
Ile1					25.2	15.5	10.7				
Ile2	58.8	36.5	175.2			15.3					
Val1	61.6	29.9		121.3	19.2						
Val2	59.9	30.7		121.2	19.0						
Val3	56.1	31.8	172.5		18.5						
Val4	58.1		173.7		19.5						
Val5		30.0			20.4						
Gln/Glu1	53.5	30.8		126.1	27.8		184.6				
Phe/Tyr1	55.5	38.2		121.9							
Ala1	48.1		17.2	117.2							
Ala2	51.5	19.6		128.5							
Ala3	52.4	19.8									
Leu1	52.2				23.1	24.6					

Table S4. Solid-state NMR experimental parameters of microtubule-bound tau. All experiments were recorded on an 18.8 T spectrometer (800 MHz ^{1}H frequency). Reported temperatures are estimated sample temperatures based on the water ^{1}H chemical shift.

Experiment	NMR Parameters	Samples	Expt. Time
2D CC with 23-80 ms CORD mixing	T_{sample} = 278 K; ν_{MAS} = 10.5 kHz, ns = 64, τ_{rd} = 1.7 s, $_{t1,max}$ = 8.7 ms; $t_{1,inc}$ = 24.8 µs; τ_{dwell} = 6 µs; τ_{acq} = 15.4 ms; τ_{HC} = 70-800 µs; τ_{CORD} = 23-80 ms; ν_{1Hacq} = 71 kHz TPPM	MT : P2R tau (1 : 1) MT : P2R tau (1 : 0.5) Tub : P2R tau (1 : 2)	110 hr 130 hr 65 hr
2D NCA SPECCP	T_{sample} = 278 K; ν_{MAS} = 10.5 kHz, ns = 256, τ_{rd} = 1.7 s, $t_{1,max}$ = 9.5 ms; $t_{1,inc}$ = 95.2 µs; τ_{dwell} = 6 µs; τ_{acq} = 15.4 ms; τ_{HN} = 1 ms; τ_{NC} = 5.5 ms; $\nu_{15NspecificCP}$ = 26.3 kHz ramp 90-100%; $\nu_{13CspecificCP}$ = 15.8 kHz; $\nu_{1HspecificCP}$ = 71 kHz CW; ν_{1Hacq} = 71 kHz TPPM	MT : P2R tau (1 : 1) MT : P2R tau (1 : 0.5) MT : 0N4R tau (1 : 1) Tub : P2R tau (1 : 2)	50 hr 80 hr 46 hr 75 hr
2D NCO SPECCP	T_{sample} = 278 K; ν_{MAS} = 14 kHz, ns = 256/352, τ_{rd} = 1.7 s, $t_{1,max}$ = 9.3 ms; $t_{1,inc}$ = 142.9 µs; τ_{dwell} = 6 µs; τ_{acq} = 15.4 ms; τ_{HN} = 3 ms; τ_{NC} = 5 ms; $\nu_{15NspecificCP}$ = 25.2 kHz ramp 90-100%; $\nu_{13CspecificCP}$ = 39.2 kHz; $\nu_{1HspecificCP}$ = 71 kHz CW; ν_{1Hacq} = 71 kHz TPPM	MT : P2R tau (1 : 1)	38 hr
2D N(CO)CA SPECCP-BSHCP	T_{sample} = 278 K; ν_{MAS} = 14 kHz, ns = 512, τ_{rd} = 1.7 s, $t_{1,max}$ = 6.4 ms; $t_{1,inc}$ = 142.9 µs; τ_{dwell} = 6 µs; τ_{acq} = 15.4 ms; τ_{HN} = 3 ms; τ_{NC} = 5 ms; τ_{CC} = 4.5 ms; $\nu_{15NspecificCP}$ = 25.2 kHz 90-100% ramp; $\nu_{13CspecificCP}$ = 39.2 kHz; $\nu_{1HspecificCP}$ = 71 kHz CW; ν_{1Hacq} = 83 kHz TPPM; $\nu_{1HBSHCP}$ = 90 kHz CW	MT : 0N4R tau (1 : 1)	88 hr
2D ^{1}H-^{13}C INEPT	T_{sample} = 278 K; ν_{MAS} = 10.5 kHz, ns = 112, τ_{rd} = 2 s, $t_{1,max}$ = 15.9 ms; $t_{1,inc}$ = 124.8 µs; τ_{dwell} = 6 µs; τ_{acq} = 24.6 ms; ν_{1Hacq} = 71 kHz TPPM	MT : P2R tau (1 : 1) MT : P2R tau (1 : 0.5)	17 hr 17 hr
2D N(CA)CB SPECCP-DREAM	T_{sample} = 278 K; ν_{MAS} = 14 kHz, ns = 480, τ_{rd} = 1.7 s, $t_{1,max}$ = 6.4 ms; $t_{1,inc}$ = 142.9 µs; τ_{dwell} = 6 µs; τ_{acq} = 15.4 ms; τ_{HN} = 3 ms; τ_{NC} = 5.5 ms; τ_{CC} = 2 ms; $\nu_{15NspecificCP}$ = 26.3kHz 90-100% ramp; $\nu_{13CspecificCP}$ = 15.8 kHz; $\nu_{1HspecificCP}$ = 83 kHz CW; ν_{1Hacq} = 83 kHz TPPM; $\nu_{1HDREAM}$ = 83 kHz CW	MT : 0N4R tau (1 : 1)	84 hr
1D ^{13}C DP	T_{sample} = 278 K; ν_{MAS} = 10.5 kHz, ns = 4096, τ_{rd} = 3 s, τ_{dwel} = 6 µs; τ_{acq} = 15.4 ms; ν_{1Hacq} = 83 kHz TPPM	MT : P2R tau (1 : 1) MT : P2R tau (1 : 0.5) MT : 0N4R tau (1 : 1) MT only	3.5 hr 3.5 hr 3.5 hr 3.5 hr
1D ^{13}C CP	T_{sample} = 278 K; ν_{MAS} = 10.5 kHz, ns = 4096, τ_{rd} = 1.7 s, τ_{dwel} = 6 µs; τ_{acq} = 15.3 ms; τ_{HC} = 70/800 µs; ν_{1Hacq} = 71 kHz TPPM	MT : P2R tau (1 : 1) MT : P2R tau (1 : 0.5) MT : 0N4R tau (1 : 1) MT only	2 hr 2 hr 2 hr 2 hr
1D ^{13}C INEPT	T_{sample} = 278 K; ν_{MAS} = 10.5 kHz; ns = 4096, τ_{rd} = 2 s; τ_{dwell} = 6 µs; τ_{acq} = 24.6 ms; ν_{1Hacq} = 71 kHz TPPM	MT : P2R tau (1 : 1) MT : P2R tau (1 : 0.5) MT : 0N4R tau (1 : 1) MT only	2.5 hr 2.5 hr 2.5 hr 2.5 hr
1D water-edited ^{13}C CP	T_{sample} = 278 K; ν_{MAS} = 10.5 kHz, ns = 1024, τ_{rd} = 1.7 s; τ_{dwell} = 6 µs; τ_{acq} = 15.3 ms; $\tau_{1Hselpulse}$ = 950 µs; $\tau_{T2filter}$ = 95 µs x10; τ_{SD} = 0/4/16/36/100 ms; τ_{HC} = 70 µs; ms; ν_{1Hacq} = 71 kHz TPPM	MT : P2R tau (1 : 1) MT : P2R tau (1 : 0.5) MT : 0N4R tau (1 : 1) MT only	2.5 hr 2.5 hr 2.5 hr 2.5 hr

Symbols: T_{sample} = sample temperature; ν_{MAS} = MAS frequency; ns = number of scans (transients) per free induction decay (FID); τ_{rd} = recycle delay between scans; $t_{1,max}$ = maximum t_1 (indirect dimension 1) evolution time; $t_{1,inc}$ = increment for t_1 (indirect dimension 1) evolution time; τ_{dwell} = dwell time during direct FID acquisition; τ_{acq} = maximum acquisition time during direct FID detection; τ_{XY} = cross polarization (CP, ^{SPECIFIC}CP, BSH-CP, or DREAM) contact time during CP from channel X to channel Y; $\nu_{nuc\text{-}CP,XY}$ = radiofrequency field strength for CP spin lock on *nuc* (*nuc* = ^{1}H, ^{13}C, ^{15}N) during CP from X to Y; $\nu_{1H,\ acq}$ = dipolar decoupling field strength during FID acquisition and indirect dimension evolution; $\nu_{nuc\text{-}DCP}$ = rf spin lock field strength on *nuc* during heteronuclear CP; $\nu_{1H\text{-}DD,DCP}$ = ^{1}H

dipolar decoupling field strength during heteronuclear CP; τ_{DREAM} = spin lock contact time during homonuclear coherence transfer with the DREAM condition.

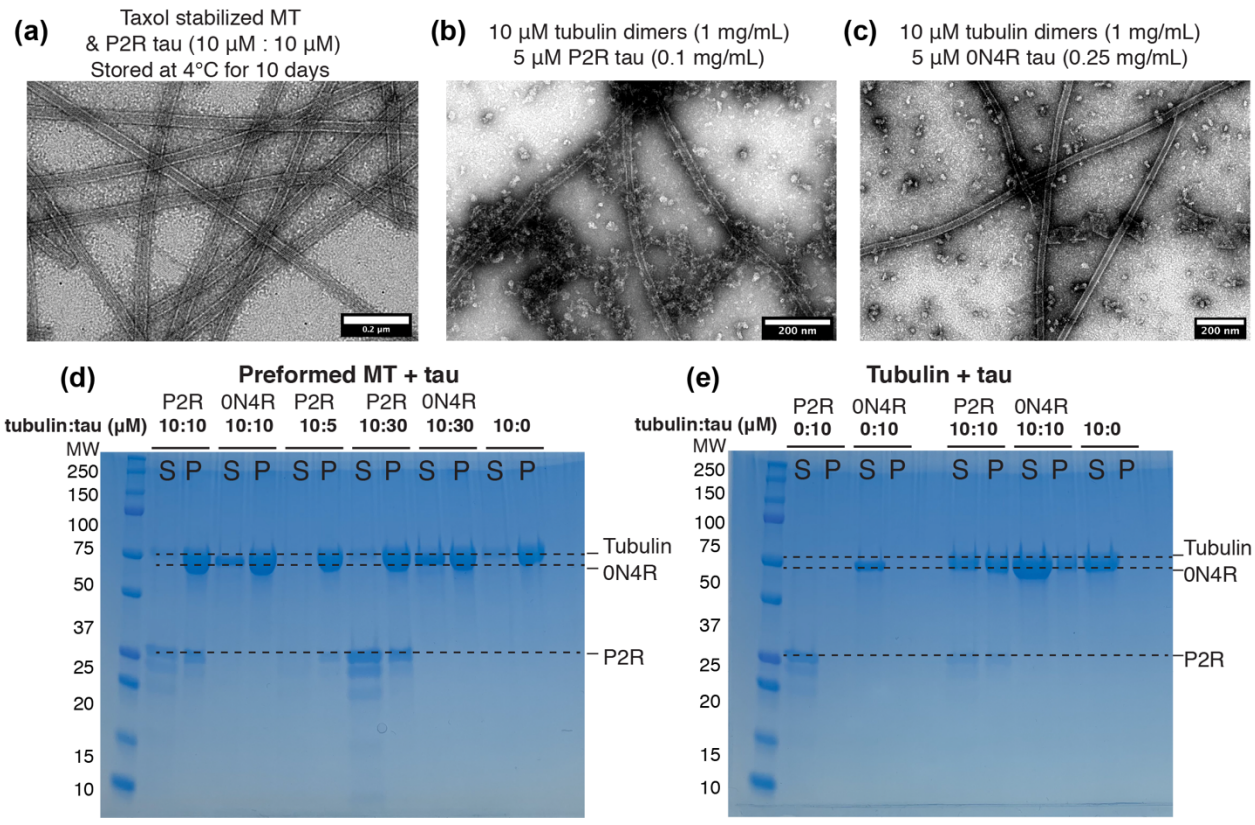

Figure S1. **Characterization of P2R tau purity and tau-tubulin interactions.** (**a**) TEM images of preformed microtubules with bound P2R tau (molar ratio 1 : 1). The sample was imaged after storage for 10 days at 4˚C as a pellet, the same condition as samples used for solid-state NMR experiments. The microtubules remain intact, indicating that the solid-state NMR samples are stable over the duration of the experiments. (**b**) TEM images of microtubules co-assembled with P2R tau at a molar ratio of 1 : 0.5 for tubulin dimers : tau in the absence of taxol. (**c**) TEM images of microtubules co-assembled with 0N4R tau at a molar ratio of 1 : 0.5 in the absence of taxol. (**d**) SDS-PAGE gel of the pellet (P) and supernatant (S) of preformed microtubules with varying concentrations of P2R tau after ultracentrifugation. Tubulin and P2R tau co-sediment into pellets, indicating that P2R tau binds microtubules. (**e**) SDS-PAGE gel of the pellet and supernatant of tubulin : tau mixtures prepared under similar conditions as those shown in (**b**) and (**c**) after ultracentrifugation.

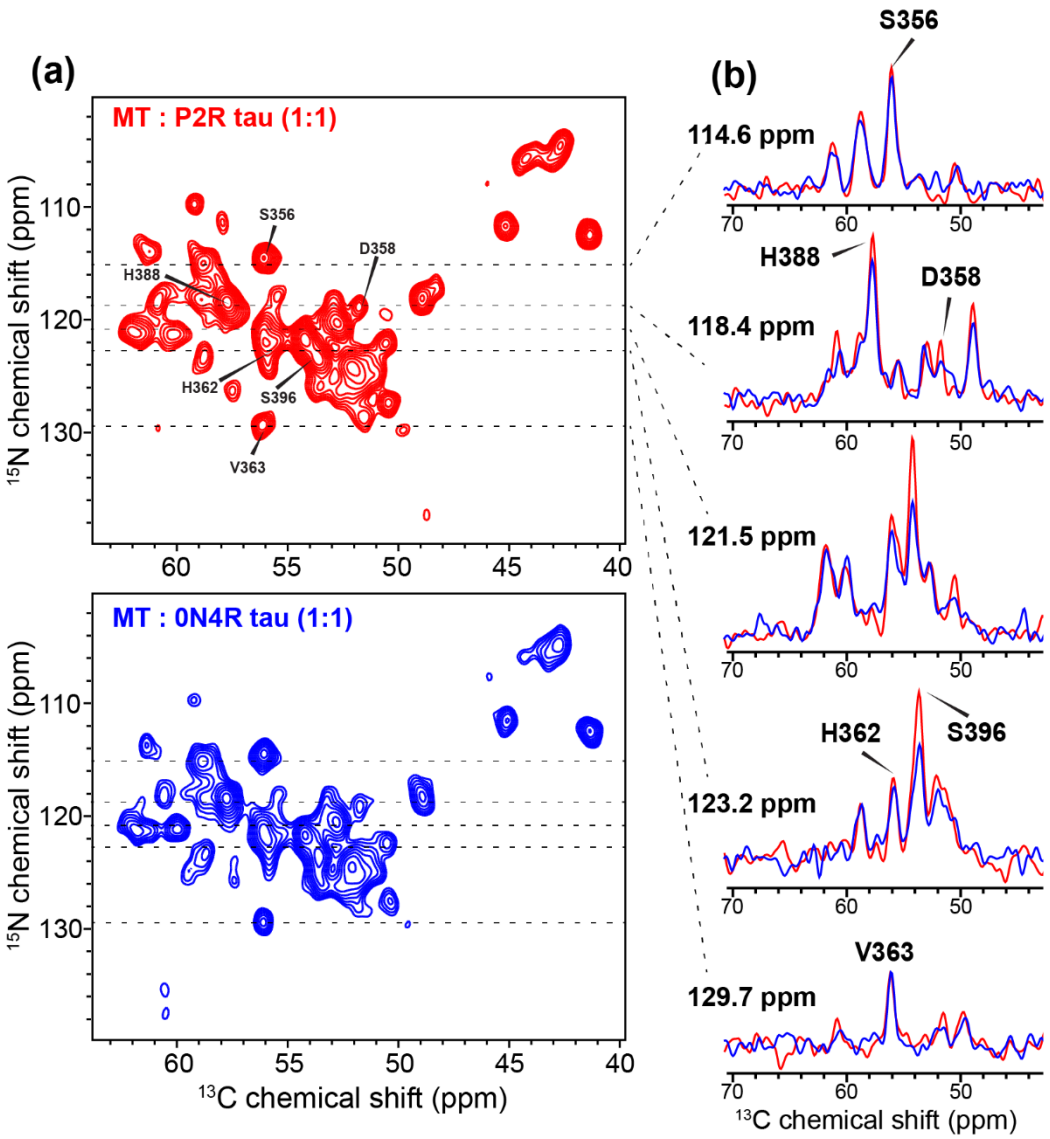

Figure S2. 1D ^{15}N cross sections of the 2D NCα spectra of microtubule-bound tau show good spectral sensitivity. (**a**) 2D spectra of P2R tau (top) and 0N4R tau (bottom) bound to microtubules at the 1 : 1 molar ratio. The 2D spectra were processed using the Gaussian window function with LB = -20 and GB=0.05. The same 2D data are also shown in Fig. 1d but were processed using a sine bell window function with SSB = 3 to better resolve some of the peaks. (**b**) Overlay of selected ^{15}N cross sections, indicating some of the sequentially assigned peaks.

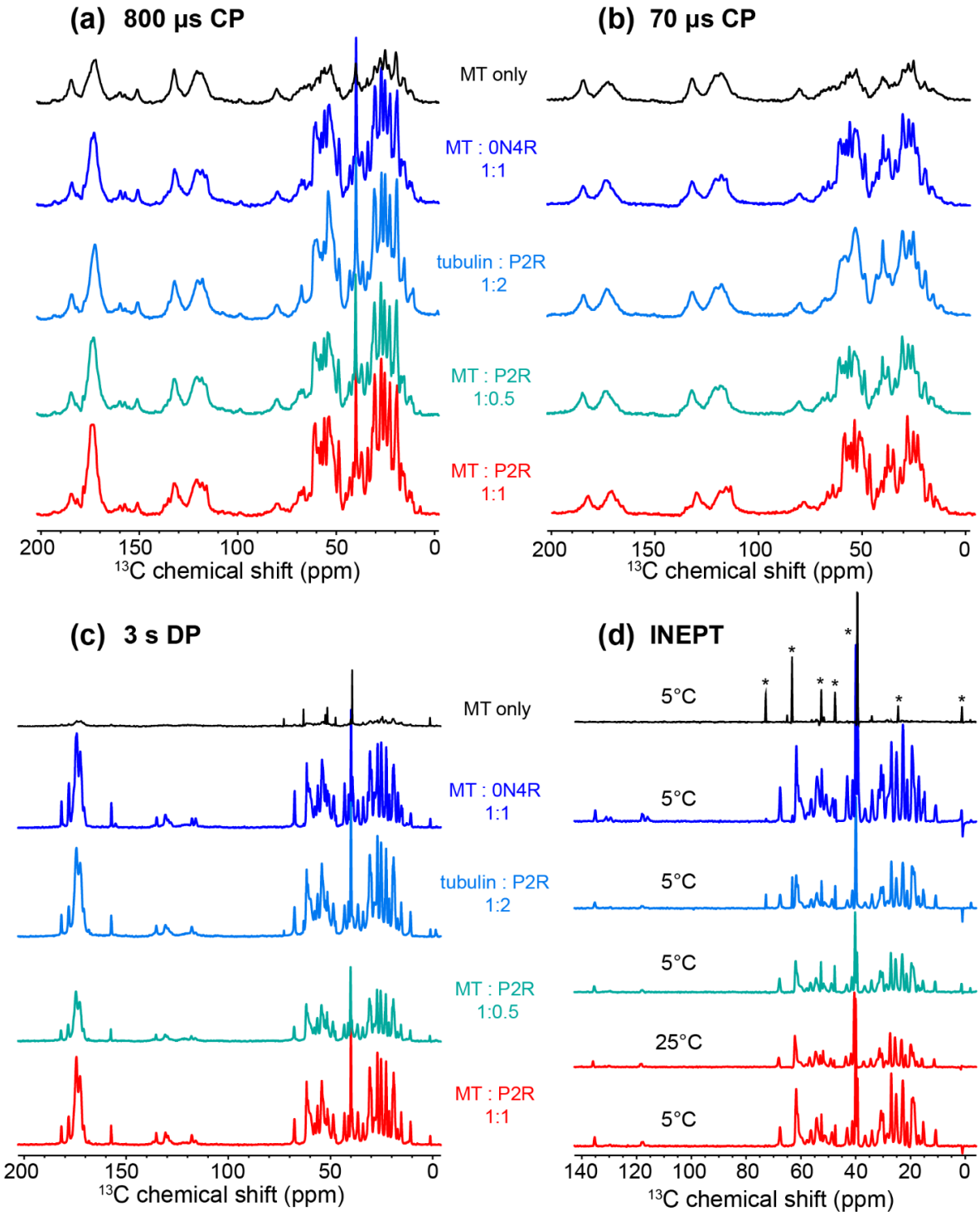

Figure S3. **^{13}C NMR spectra of microtubules with and without bound tau at varying molar ratios of microtubules and tau.** Four tau-containing samples are compared: P2R tau bound to taxol-stabilized microtubules (MT) at 1 : 1 (red) and 1 : 0.5 (green) molar ratios of tubulin heterodimers to tau, tubulin co-assembled with P2R tau at 1 : 2 molar ratio (marine blue), and taxol-stabilized MTs with bound full-length 0N4R tau at 1 : 1 ratio (royal blue). The MT-only spectra (grey) are also shown for comparison. (**a**) ^{13}C CP spectra measured with 800 µs contact time, detecting semi-rigid and rigid residues. (**b**) ^{13}C CP with 70 µs contact time, detecting highly

rigid residues. (**c**) ^{13}C DP spectra measured with a 3 s recycle delay. These spectra reflect nearly quantitative intensities of all the residues. (**d**) ^{13}C INEPT spectra, detecting nearly isotropically mobile residues. Most spectra were measured on the 800 MHz NMR at ~5˚C. The 25˚C INEPT spectrum of the 1 : 1 MT : P2R tau sample has very similar intensity patterns as the 5˚C spectrum, indicating that the INEPT-detected residues are dynamic even at 5˚C. Asterisks in the MT-only INEPT spectrum indicate the signals of solvents, buffer salt and small molecules such as glycerol, PIPES, DMSO, and DSS. All molar ratios refer to tubulin heterodimers to tau, and all samples contained 10 μM taxol-stabilized microtubules (MT) or tubulin co-assembled with tau.

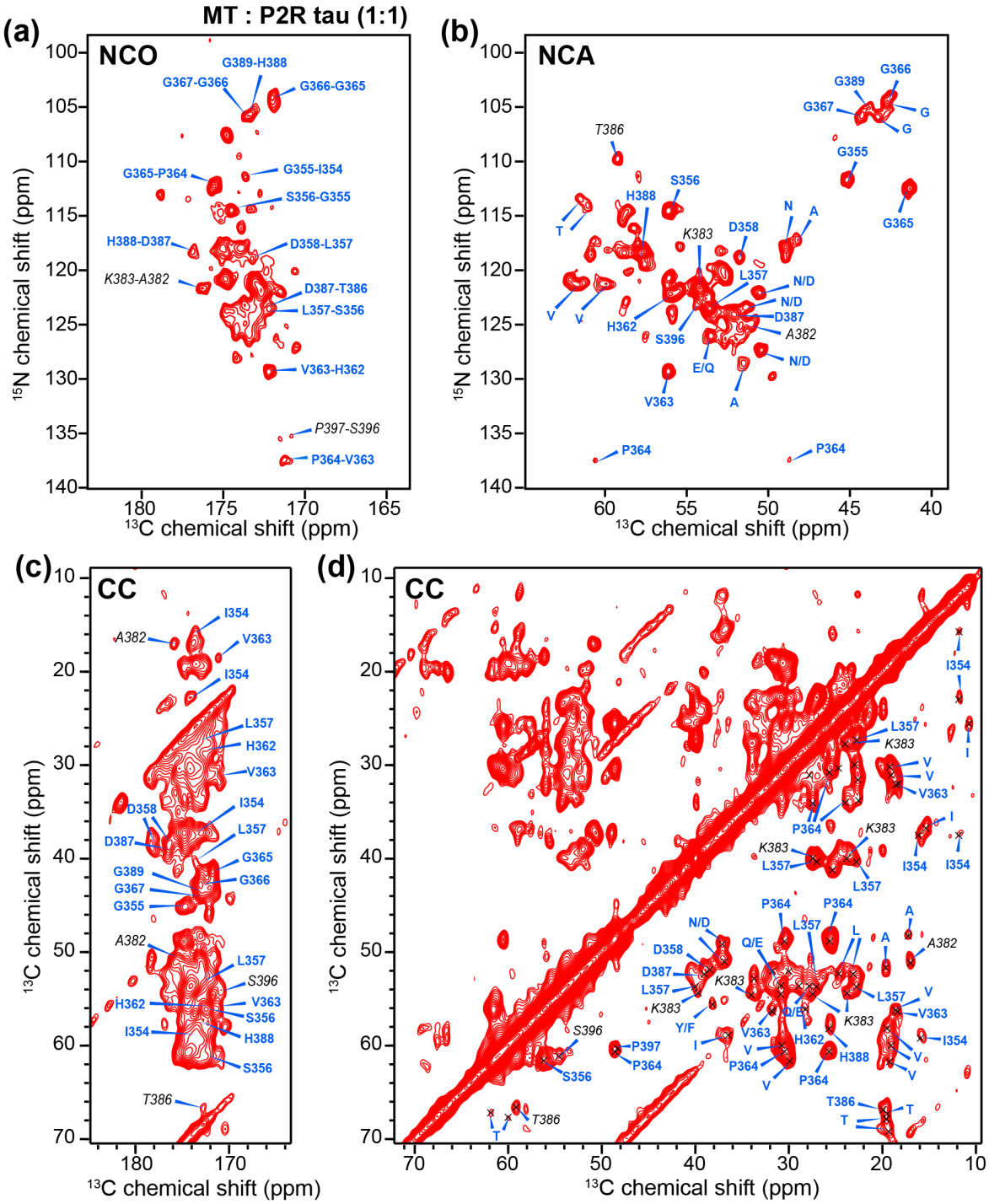

Figure S4. **^{15}N and ^{13}C chemical shifts of microtubule-bound P2R tau (1 : 1) from 2D ^{15}N-^{13}C and ^{13}C-^{13}C correlation spectra**. Unambiguous assignments are shown in blue while ambiguous assignments are shown in black italics. (**a**) Inter-residue 2D NCO spectra. (**b**) Intra-residue 2D NCα spectrum reproduced from Figure 1d. These 2D NC spectra were processed using a sine bell window function with SSB = 2. (**c**) Carbonyl region of the 50 ms 2D ^{13}C-^{13}C CORD spectrum. (**d**) Aliphatic region of the 50 ms 2D CC spectrum. The CC spectrum was processed using a Gaussian window function with LB = -30 and GB = 0.05 for both dimensions.

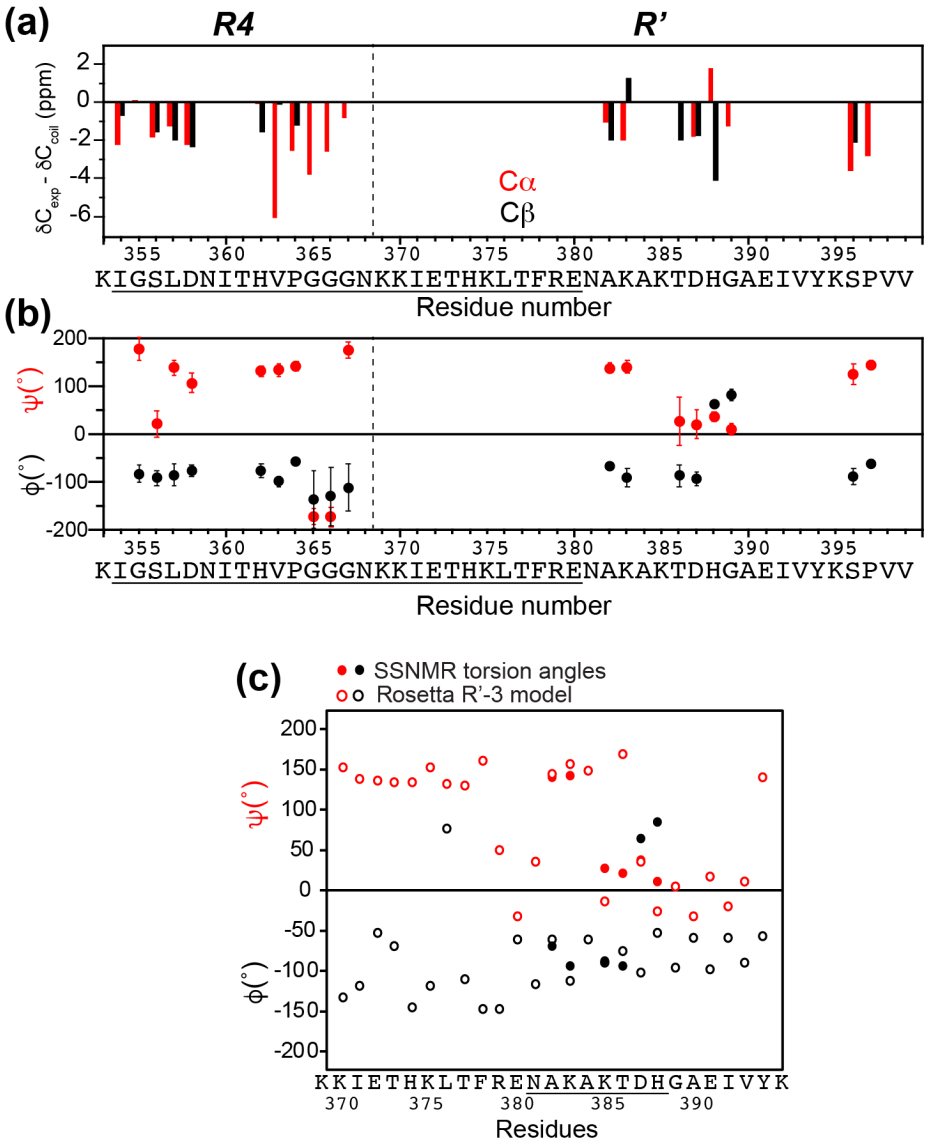

Figure S5. **Backbone conformation of microtubule-bound P2R tau (1 : 1) residues**. (**a**) Cα and Cβ secondary chemical shifts. Residues ^{353}Lys-Gly^{367} and ^{381}Asn-Val^{399} form two stretches with largely assigned chemical shifts. (**b**) (ϕ, ψ) torsion angles obtained from the NMR chemical shifts. (**c**) Comparison of the chemical-shift derived torsion angles (filled circles) with the Rosetta refined torsion angles (open circles) for ^{369}Lys-Val^{395} (see analysis in **Fig. S10**) The two results agree well for residues ^{381}NAKAKTDH^{388}.

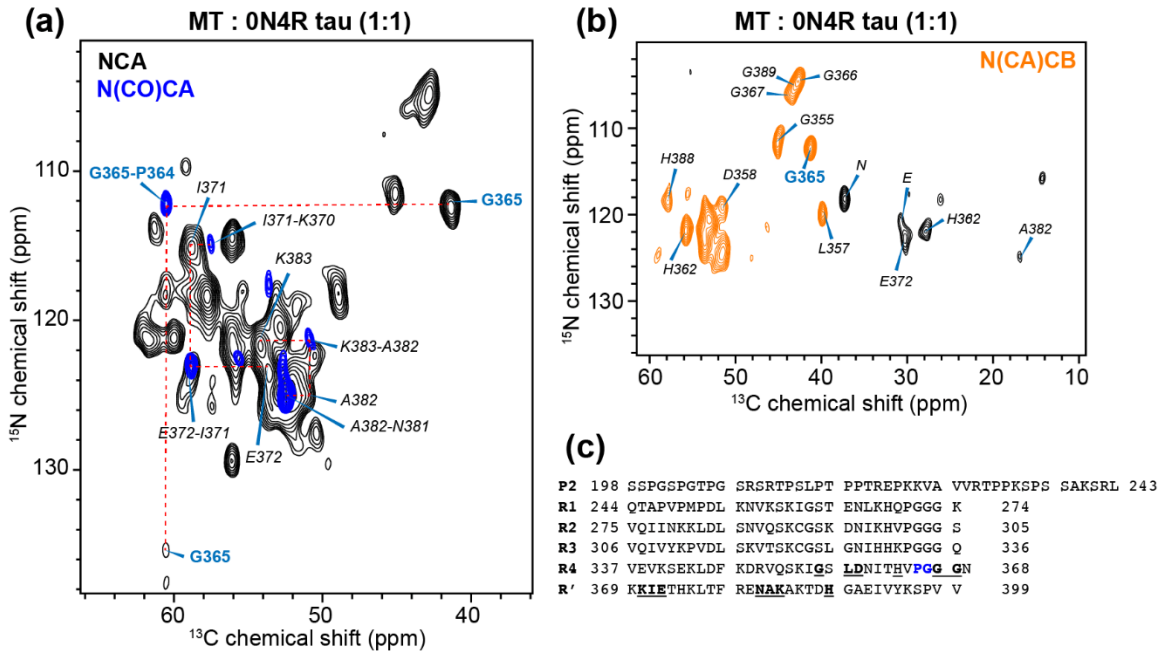

Figure S6. **^{15}N and ^{13}C chemical shift assignment of taxol-stabilized microtubule-bound 0N4R tau (1 : 1)**. (**a**) Overlay of the 2D NCα (black) and N(CO)CA (blue) spectrum. Sequential assignments are shown in blue. Ambiguous assignments are italicized and shown in black. (**b**) 2D N(CA)CB spectrum. Positive signals are in orange and negative Cβ signals are in black. The Cβ cross peaks confirm some of the sequential assignments for the MT-bound P2R tau sample (1 : 1). (**c**) Amino acid sequence of the five repeats of tau. Unambiguously assigned residues are shown in blue. Sequential assignments that are ambiguous or made by comparison with MT-bound P2R tau (1 : 1) are underlined.

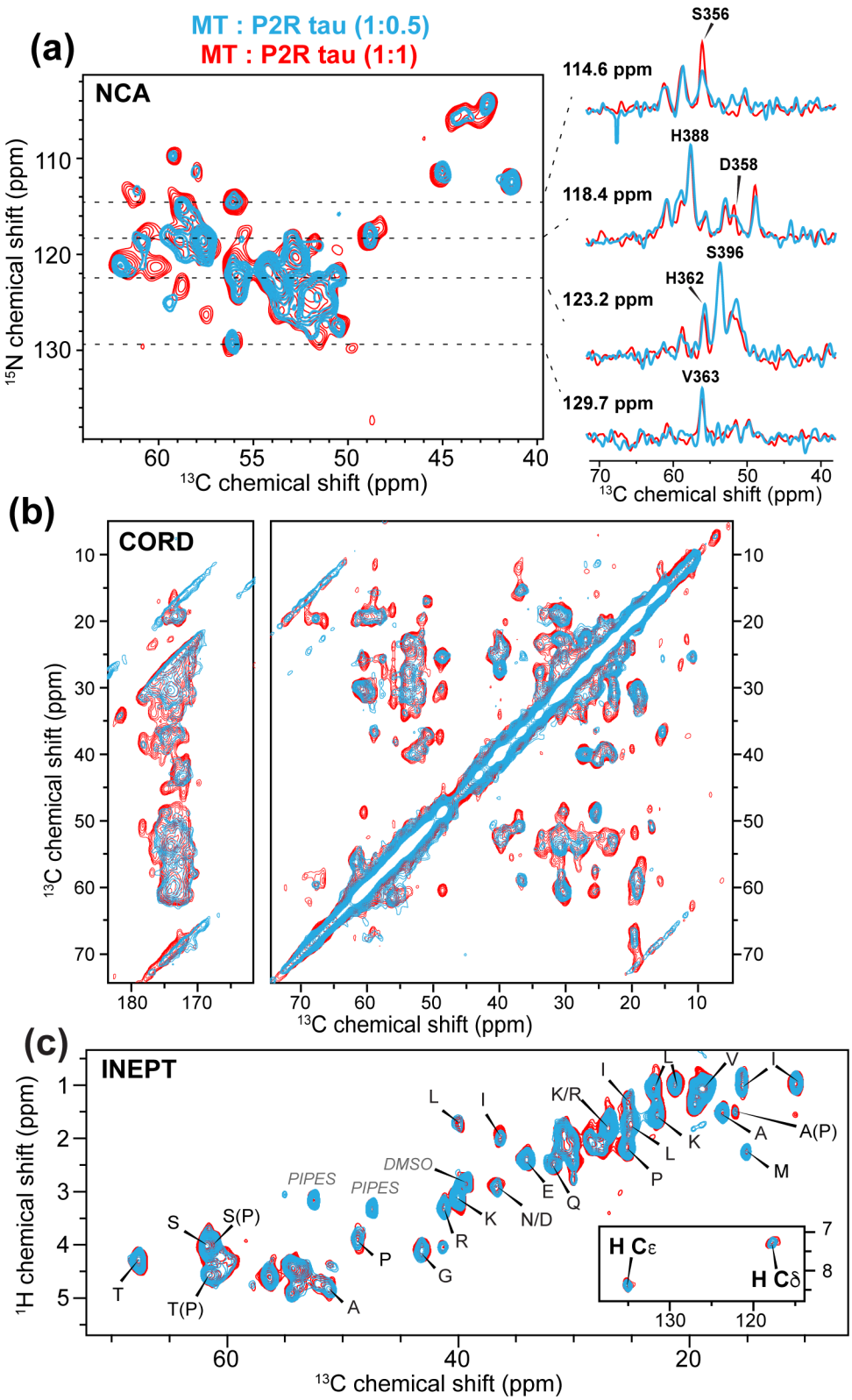

Figure S7. **Taxol-stabilized microtubule-bound P2R tau adopts the same conformation at 1 : 1 and 1 : 0.5 ratios of tubulin heterodimer : tau**. (**a**) 2D NCα spectra of the 1 : 1 (red) and 1 : 0.5 (cyan) samples and representative 1D cross sections at various ^{15}N chemical shifts. The spectral

patterns are similar between the two samples, indicating that the tau-MT interaction observed in the 1 : 1 sample is not due to crowding, and the bound domain has the same conformation at the two molar ratios. The MT concentrations were 10 μM before packing into the MAS rotors. (**b**) 2D CC spectra of the 1 : 1 (red) and 1 : 0.5 (green) samples, measured with 50 ms ^{13}C spin diffusion at ~280 K under 10.5 kHz MAS. (**c**) 2D ^{1}H-^{13}C INEPT spectrum of the 1 : 0.5 sample (green) compared to the 1 : 1 sample (red).

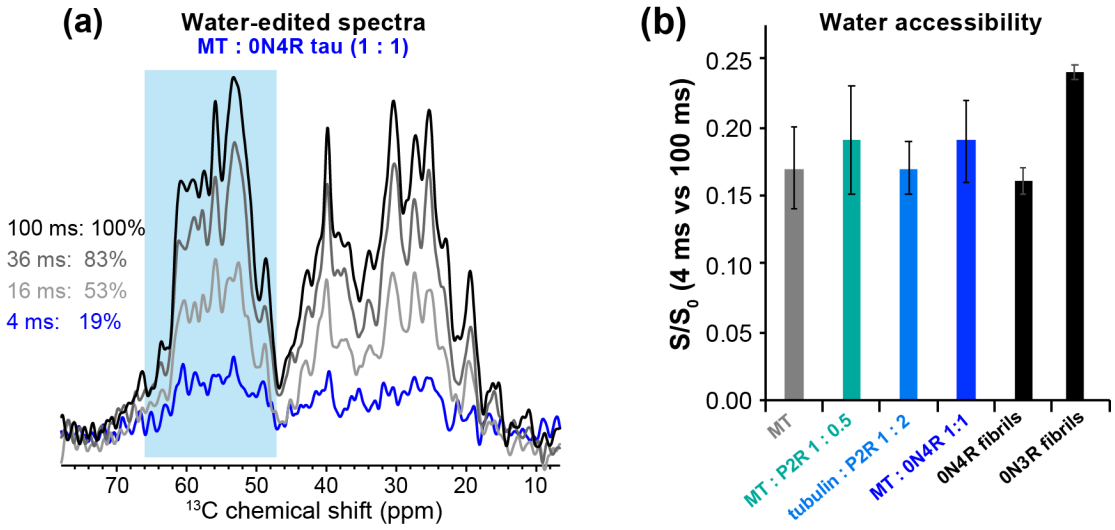

Figure S8. **Microtubule-bound tau is shielded from water**. (**a**) Water-edited ^{13}C spectra of MT-bound 0N4R tau (1 : 1), measured with ^{1}H spin diffusion mixing times of 4, 16, 36, and 100 ms. Intensity ratios are integrated over 46-71 ppm. (**b**) Water-edited intensity ratios between 4 ms and 100 ms ^{1}H mixing for various MT-bound tau samples compared with previously reported water-edited intensities of heparin-fibrilized 0N4R tau (*19, 20*) and 0N3R tau fibrils (*21*). The rigid domain of MT-bound tau is dehydrated: its S/S_0 value of ~0.19 is similar to the 0N4R and 0N3R tau fibrils' S/S_0 values of ~0.15 and 0.23.

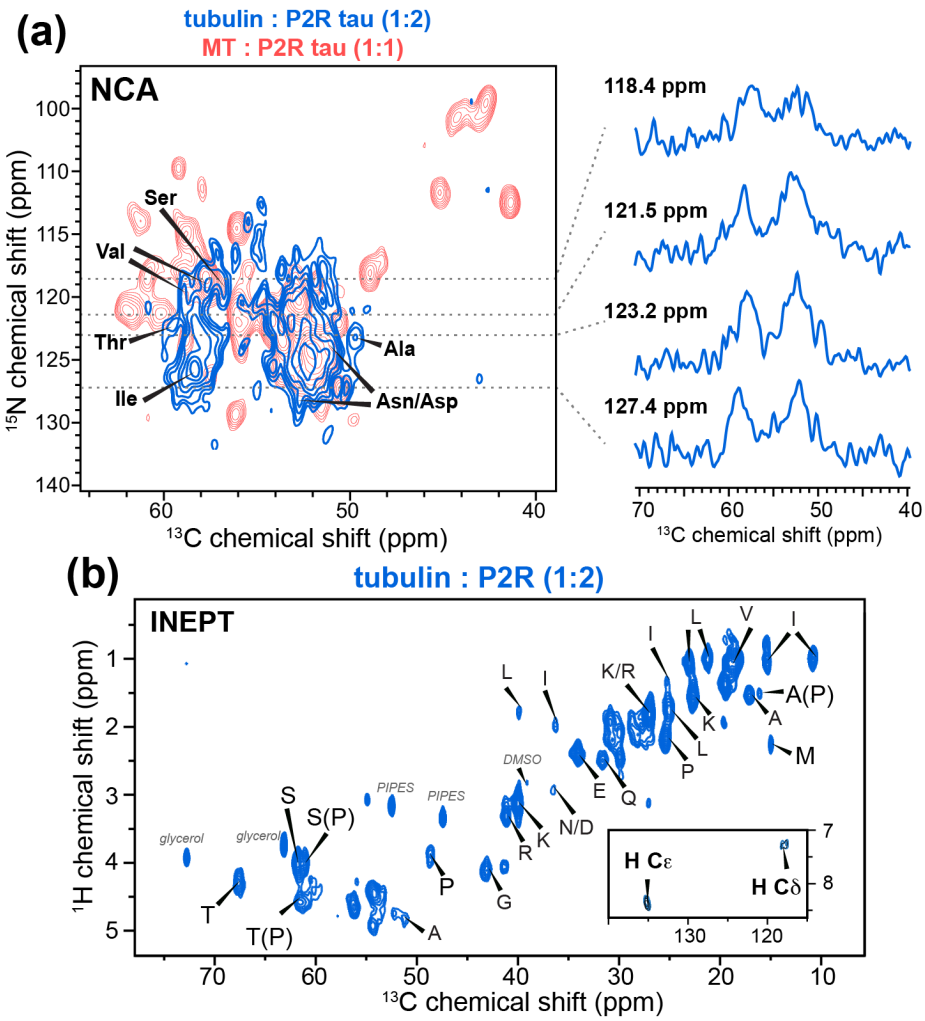

Figure S9. **2D spectra of tubulin : P2R tau (1 : 2) co-assembled sample indicate that tau binds dynamically unstable microtubules via the R' repeat.** (**a**) 2D dipolar NCα spectrum of the tubulin : P2R tau co-assembled sample (blue, same as **Fig. 3a**) and its 1D ^{15}N cross sections. The 2D spectrum of the taxol-stabilized MT-P2R tau (1 : 1) sample is overlaid in red (same as **Fig. 1d**) for comparison. (**b**) 2D ^{1}H-^{13}C INEPT spectrum of the tubulin – tau co-assembled sample with residue type assignment. The aromatic region of the 2D spectrum (inset) exhibits His signals but lacks Phe and Tyr signals.

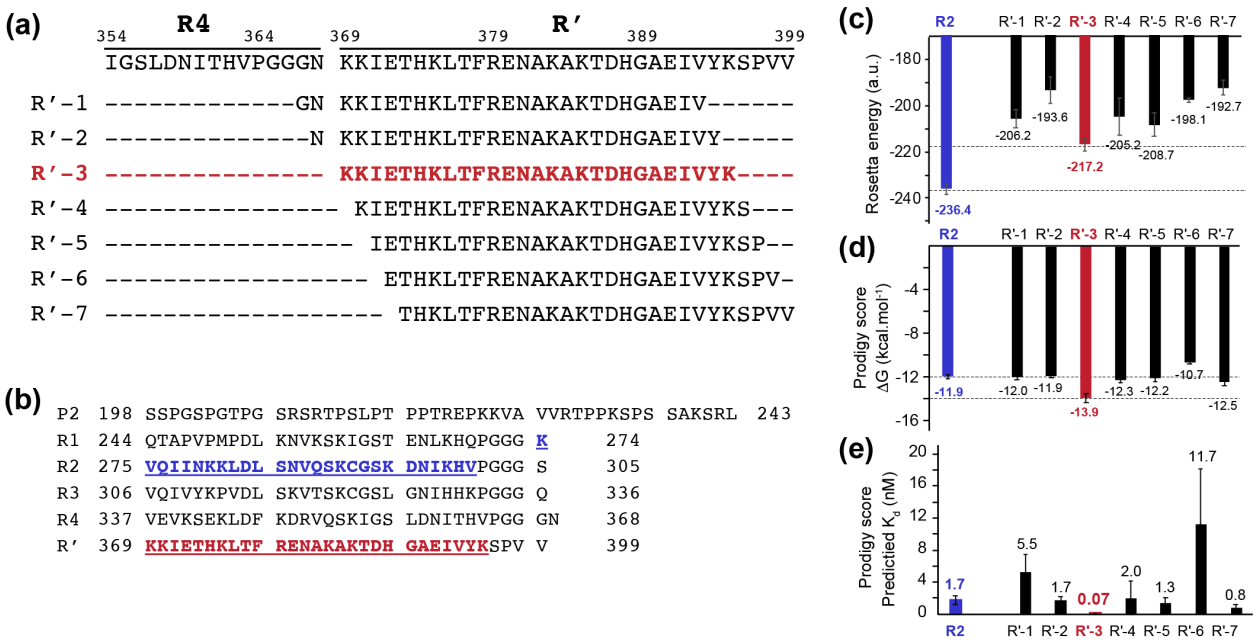

Figure S10. **Structure modeling of microtubule-bound R'(369-395) using NMR chemical shifts, cryo-EM density, and Rosetta**. (**a**) Seven 27-residue sequences in R' tested using Rosetta. The sequences are chosen based on NMR spectra showing that PGGG is excluded from the rigid domain and cryo-EM data that indicate 27 residues bound to the MT. (**b**) Amino acid sequence of P2R tau. R2(274-300) is shown in blue and R'(369-395) is shown in red. (**c**) Rosetta energy scores of the seven R' sequences against the electron densities (EMD-7771) obtained for the chimera tau construct R2 x 4. A R2(274-300) tau model (blue) was generated for comparison. Among the seven R' sequences, R'-3 gives the lowest energy. (**d**) Prodigy scores (*26*) of the 5 models with the lowest Rosetta energies for each sequence to assess binding affinities. R'-3 has the lowest ΔG (kcal.mol^{-1}) value. (**e**) Predicted K_d values for each 27-residue segment. R'-3 has the highest affinity (lowest K_d) to microtubules. Error bars in (c-e) are calculated based on the standard deviation of the 5 best models.

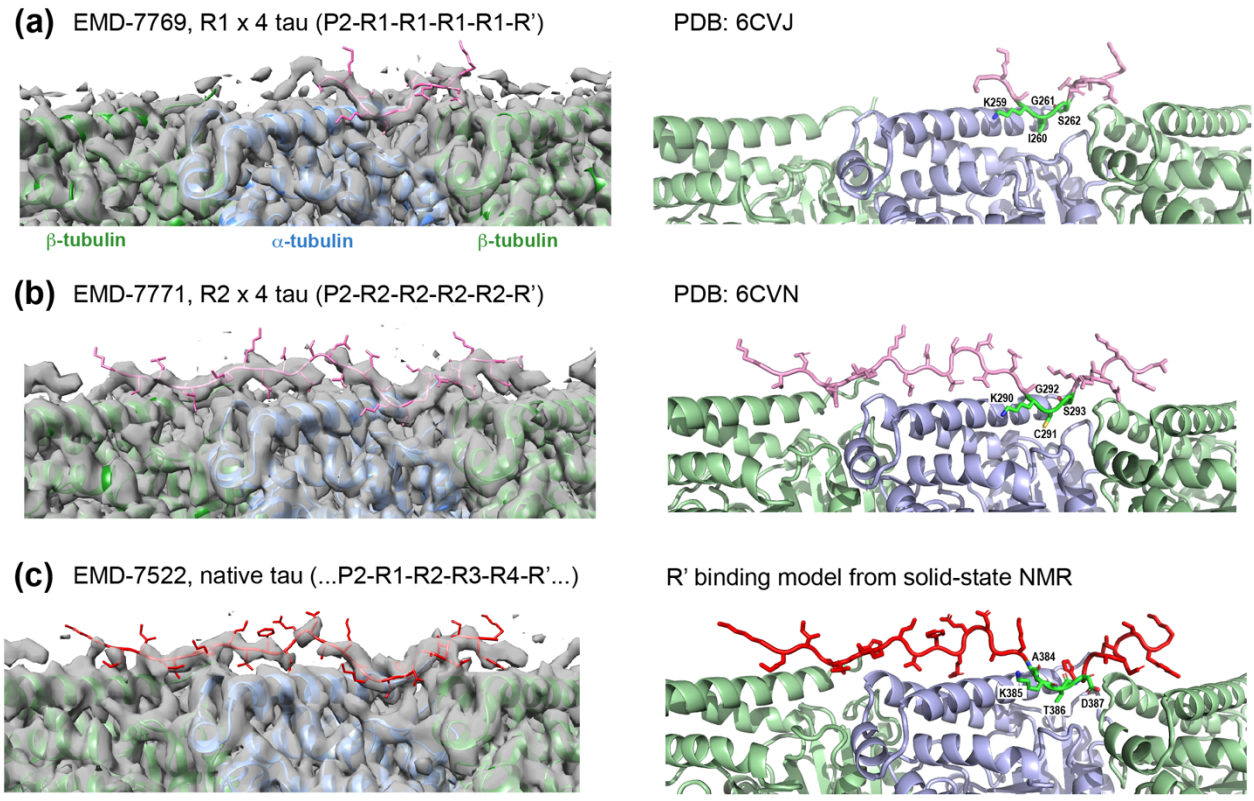

Figure S11. **Structural models of the microtubule-binding domains in chimeric tau versus the microtubule-binding domain in wild-type tau.** Cryo-EM density maps of three different tau constructs reported before (*14*) are shown on the left and the Rosetta-refined structures are shown on the right. (**a**) Electron density map (EMD-7769) of chimeric R1 x 4 tau best matches a 12-residue segment from V256 to K267, whose lowest energy structure model is shown on the right (pink). (**b**) Electron density map (EMD-7771) of chimeric R2 x 4 tau best matches a 27-residue segment from K274 to V300, whose lowest energy structure model (PDB: 6CVN) is shown on the right (pink). (**c**) Electron density map (EMD-7752) of wild-type tau overlaid with NMR chemical-shifts-constrained and Rosetta-refined R' lowest-energy model. This R' segment, K369 to K395, is constrained by the measured chemical shifts of the immobilized residues in the dipolar correlation solid-state NMR spectra shown here. In each of the three structural models, the four residues that show the closest approach to microtubules are indicated. These are ^{259}KIGS^{262} in R1, ^{290}KCGS^{293} in R2, and ^{384}AKTD^{387} in R'.

REFERENCES AND NOTES

1. G. M. Alushin, G. C. Lander, E. H. Kellogg, R. Zhang, D. Baker, E. Nogales, High-resolution microtubule structures reveal the structural transitions in αβ-tubulin upon GTP hydrolysis. *Cell* **157**, 1117–1129 (2014).

2. M. D. Weingarten, A. H. Lockwood, S. Y. Hwo, M. W. Kirschner, A protein factor essential for microtubule assembly. *Proc. Natl. Acad. Sci. U.S.A.* **72**, 1858–1862 (1975).

3. Y. Wang, E. Mandelkow, Tau in physiology and pathology. *Nat. Rev. Neurosci.* **17**, 5–21 (2016).

4. M. Hong, V. Zhukareva, V. Vogelsberg-Ragaglia, Z. Wszolek, L. Reed, B. I. Miller, D. H. Geschwind, T. D. Bird, D. McKeel, A. Goate, J. C. Morris, K. C. Wilhelmsen, G. D. Schellenberg, J. Q. Trojanowski, V. M. Lee, Mutation-specific functional impairments in distinct tau isoforms of hereditary FTDP-17. *Science* **282**, 1914–1917 (1998).

5. G. T. Bramblett, M. Goedert, R. Jakes, S. E. Merrick, J. Q. Trojanowski, V. M. Lee, Abnormal tau phosphorylation at Ser^{396} in Alzheimer's disease recapitulates development and contributes to reduced microtubule binding. *Neuron* **10**, 1089–1099 (1993).

6. E. M. Mandelkow, E. Mandelkow, Biochemistry and cell biology of tau protein in neurofibrillary degeneration. *Cold Spring Harb. Perspect. Med.* **2**, a006247 (2012).

7. M. Goedert, R. Jakes, M. G. Spillantini, M. Hasegawa, M. J. Smith, R. A. Crowther, Assembly of microtubule-associated protein tau into Alzheimer-like filaments induced by sulphated glycosaminoglycans. *Nature* **383**, 550–553 (1996).

8. M. E. Orr, A. C. Sullivan, B. Frost, A brief overview of tauopathy: Causes, consequences, and therapeutic strategies. *Trends Pharmacol. Sci.* **38**, 637–648 (2017).

9. N. Gustke, B. Trinczek, J. Biernat, E. M. Mandelkow, E. Mandelkow, Domains of tau protein and interactions with microtubules. *Biochemistry* **33**, 9511–9522 (1994).

10. H. Kadavath, R. V. Hofele, J. Biernat, S. Kumar, K. Tepper, H. Urlaub, E. Mandelkow, M. Zweckstetter, Tau stabilizes microtubules by binding at the interface between tubulin heterodimers. *Proc. Natl. Acad. Sci. U.S.A.* **112**, 7501–7506 (2015).

11. B. Gigant, I. Landrieu, C. Fauquant, P. Barbier, I. Huvent, J. M. Wieruszeski, M. Knossow, G. Lippens, Mechanism of tau-promoted microtubule assembly as probed by NMR spectroscopy. *J. Am. Chem. Soc.* **136**, 12615–12623 (2014).

12. K. M. McKibben, E. Rhoades, Independent tubulin binding and polymerization by the proline-rich region of tau is regulated by tau's N-terminal domain. *J. Biol. Chem.* **294**, 19381–19394 (2019).

13. J. Al-Bassam, R. S. Ozer, D. Safer, S. Halpain, R. A. Milligan, MAP2 and tau bind longitudinally along the outer ridges of microtubule protofilaments. *J. Cell Biol.* **157**, 1187–1196 (2002).

14. E. H. Kellogg, N. M. A. Hejab, S. Poepsel, K. H. Downing, F. DiMaio, E. Nogales, Near-atomic model of microtubule-tau interactions. *Science* **360**, 1242–1246 (2018).

15. B. Reif, S. E. Ashbrook, L. Emsley, M. Hong, Solid-state NMR spectroscopy. *Nat. Rev. Methods Primers* **1**, 2 (2021).

16. Y. Luo, S. Xiang, P. J. Hooikaas, L. van Bezouwen, A. S. Jijumon, C. Janke, F. Forster, A. Akhmanova, M. Baldus, Direct observation of dynamic protein interactions involving human microtubules using solid-state NMR spectroscopy. *Nat. Commun.* **11**, 18 (2020).

17. S. Yan, H. Zhang, G. Hou, S. Ahmed, J. C. Williams, T. Polenova, Internal dynamics of dynactin CAP-Gly is regulated by microtubules and plus end tracking protein EB1. *J. Biol. Chem.* **290**, 1607–1622 (2015).

18. D. L. Gard, M. W. Kirschner, Microtubule assembly in cytoplasmic extracts of *Xenopus oocytes* and eggs. *J. Cell Biol.* **105**, 2191–2201 (1987).

19. A. J. Dregni, P. Duan, M. Hong, Hydration and dynamics of full-length tau amyloid fibrils investigated by solid-state nuclear magnetic resonance. *Biochemistry* **59**, 2237–2248 (2020).

20. A. J. Dregni, V. S. Mandala, H. Wu, M. R. Elkins, H. K. Wang, I. Hung, W. F. DeGrado, M. Hong, In vitro 0N4R tau fibrils contain a monomorphic β-sheet core enclosed by dynamically heterogeneous fuzzy coat segments. *Proc. Natl. Acad. Sci. U.S.A.* **116**, 16357–16366 (2019).

21. A. J. Dregni, H. K. Wang, H. Wu, P. Duan, J. Jin, W. F. DeGrado, M. Hong, Inclusion of the C-terminal domain in the β-sheet core of heparin-fibrillized three-repeat tau protein revealed by solid-state nuclear magnetic resonance spectroscopy. *J. Am. Chem. Soc.* **143**, 7839–7851 (2021).

22. S. W. Manka, C. A. Moores, Microtubule structure by cryo-EM: Snapshots of dynamic instability. *Essays Biochem.* **62**, 737–751 (2018).

23. H. Kadavath, Y. Cabrales Fontela, M. Jaremko, L. Jaremko, K. Overkamp, J. Biernat, E. Mandelkow, M. Zweckstetter, The binding mode of a tau peptide with tubulin. *Angew. Chem. Int. Ed. Engl.* **57**, 3246–3250 (2018).

24. E. Nogales, S. G. Wolf, K. H. Downing, Structure of the alpha beta tubulin dimer by electron crystallography. *Nature* **391**, 199–203 (1998).

25. S. J. Fleishman, A. Leaver-Fay, J. E. Corn, E. M. Strauch, S. D. Khare, N. Koga, J. Ashworth, P. Murphy, F. Richter, G. Lemmon, J. Meiler, D. Baker, RosettaScripts: A scripting language interface to the Rosetta macromolecular modeling suite. *PLOS ONE* **6**, e20161 (2011).

26. L. C. Xue, J. P. Rodrigues, P. L. Kastritis, A. M. Bonvin, A. Vangone, PRODIGY: A web server for predicting the binding affinity of protein-protein complexes. *Bioinformatics* **32**, 3676–3678 (2016).

27. N. Hirokawa, Y. Shiomura, S. Okabe, Tau proteins: The molecular structure and mode of binding on microtubules. *J. Cell Biol.* **107**, 1449–1459 (1988).

28. B. Niewidok, M. Igaev, F. Sundermann, D. Janning, L. Bakota, R. Brandt, Presence of a carboxy-terminal pseudorepeat and disease-like pseudohyperphosphorylation critically influence tau's interaction with microtubules in axon-like processes. *Mol. Biol. Cell* **27**, 3537–3549 (2016).

29. X. H. Li, E. Rhoades, Heterogeneous tau-tubulin complexes accelerate microtubule polymerization. *Biophys. J.* **112**, 2567–2574 (2017).

30. E. M. Mandelkow, J. Biernat, G. Drewes, N. Gustke, B. Trinczek, E. Mandelkow, Tau domains, phosphorylation, and interactions with microtubules. *Neurobiol. Aging* **16**, 355–362 (1995).

31. U. Preuss, J. Biernat, E. M. Mandelkow, E. Mandelkow, The "jaws" model of tau-microtubule interaction examined in CHO cells. *J. Cell Sci.* **110** (Pt. 6), 789–800 (1997).

32. M. D. Mukrasch, M. von Bergen, J. Biernat, D. Fischer, C. Griesinger, E. Mandelkow, M. Zweckstetter, The "jaws" of the tau-microtubule interaction. *J. Biol. Chem.* **282**, 12230–12239 (2007).

33. M. Gui, H. Farley, P. Anujan, J. R. Anderson, D. W. Maxwell, J. B. Whitchurch, J. J. Botsch, T. Qiu, S. Meleppattu, S. K. Singh, Q. Zhang, J. Thompson, J. S. Lucas, C. D. Bingle, D. P. Norris, S. Roy, A. Brown, De novo identification of mammalian ciliary motility proteins using cryo-EM. *Cell* **184**, 5791–5806.e19 (2021).

34. X. Wang, Y. Fu, W. L. Beatty, M. Ma, A. Brown, L. D. Sibley, R. Zhang, Cryo-EM structure of cortical microtubules from human parasite *Toxoplasma gondii* identifies their microtubule inner proteins. *Nat. Commun.* **12**, 3065 (2021).

35. M. R. Sawaya, S. Sambashivan, R. Nelson, M. I. Ivanova, S. A. Sievers, M. I. Apostol, M. J. Thompson, M. Balbirnie, J. J. Wiltzius, H. T. McFarlane, A. Ø. Madsen, C. Riekel, D. Eisenberg, Atomic structures of amyloid cross-beta spines reveal varied steric zippers. *Nature* **447**, 453–457 (2007).

36. H. Wesseling, W. Mair, M. Kumar, C. N. Schlaffner, S. Tang, P. Beerepoot, B. Fatou, A. J. Guise, L. Cheng, S. Takeda, J. Muntel, M. S. Rotunno, S. Dujardin, P. Davies, K. S. Kosik, B. L. Miller, S. Berretta, J. C. Hedreen, L. T. Grinberg, W. W. Seeley, B. T. Hyman, H. Steen, J. A. Steen, Tau PTM profiles identify patient heterogeneity and stages of Alzheimer's disease. *Cell* **183**, 1699–1713.e13 (2020).

37. B. Falcon, J. Zivanov, W. Zhang, A. G. Murzin, H. J. Garringer, R. Vidal, R. A. Crowther, K. L. Newell, B. Ghetti, M. Goedert, S. H. W. Scheres, Novel tau filament fold in chronic traumatic encephalopathy encloses hydrophobic molecules. *Nature* **568**, 420–423 (2019).

38. A. W. P. Fitzpatrick, B. Falcon, S. He, A. G. Murzin, G. Murshudov, H. J. Garringer, R. A. Crowther, B. Ghetti, M. Goedert, S. H. W. Scheres, Cryo-EM structures of tau filaments from Alzheimer's disease. *Nature* **547**, 185–190 (2017).

39. W. Zhang, A. Tarutani, K. L. Newell, A. G. Murzin, T. Matsubara, B. Falcon, R. Vidal, H. J. Garringer, Y. Shi, T. Ikeuchi, S. Murayama, B. Ghetti, M. Hasegawa, M. Goedert, S. H. W. Scheres, Novel tau filament fold in corticobasal degeneration. *Nature* **580**, 283–287 (2020).

40. M. Castoldi, A. V. Popov, Purification of brain tubulin through two cycles of polymerization-depolymerization in a high-molarity buffer. *Protein Expr. Purif.* **32**, 83–88 (2003).

41. A. Böckmann, C. Gardiennet, R. Verel, A. Hunkeler, A. Loquet, G. Pintacuda, L. Emsley, B. H. Meier, A. Lesage, Characterization of different water pools in solid-state NMR protein samples. *J. Biomol. NMR* **45**, 319–327 (2009).

42. M. Baldus, A. T. Petkova, J. Herzfeld, R. G. Griffin, Cross polarization in the tilted frame: Assignment and spectral simplification in heteronuclear spin systems. *Mol. Phys.* **95**, 1197–1207 (1998).

43. S. A. McNeill, P. L. Gor'kov, K. Shetty, W. W. Brey, J. R. Long, A low-E magic angle spinning probe for biological solid state NMR at 750 MHz. *J. Magn. Reson.* **197**, 135–144 (2009).

44. G. Hou, S. Yan, S. Sun, Y. Han, I. J. Byeon, J. Ahn, J. Concel, A. Samoson, A. M. Gronenborn, T. Polenova, Spin diffusion driven by R-symmetry sequences: Applications to homonuclear correlation spectroscopy in MAS NMR of biological and organic solids. *J. Am. Chem. Soc.* **133**, 3943–3953 (2011).

45. J. Hoffmann, J. Ruta, C. W. Shi, K. Hendriks, V. Chevelkov, W. T. Franks, H. Oschkinat, K. Giller, S. Becker, A. Lange, Protein resonance assignment by BSH-CP-based 3D solid-state NMR experiments: A practical guide. *Magn. Reson. Chem.* **58**, 445–465 (2020).

46. S. P. Skinner, R. H. Fogh, W. Boucher, T. J. Ragan, L. G. Mureddu, G. W. Vuister, CcpNmr AnalysisAssign: A flexible platform for integrated NMR analysis. *J. Biomol. NMR* **66**, 111–124 (2016).

47. Y. Shen, A. Bax, Protein backbone and sidechain torsion angles predicted from NMR chemical shifts using artificial neural networks. *J. Biomol. NMR* **56**, 227–241 (2013).

48. J. K. Williams, M. Hong, Probing membrane protein structure using water polarization transfer solid-state NMR. *J. Magn. Reson.* **247**, 118–127 (2014).

49. T. Wang, H. Jo, W. F. DeGrado, M. Hong, Water distribution, dynamics, and interactions with Alzheimer's β-amyloid fibrils investigated by solid-state NMR. *J. Am. Chem. Soc.* **139**, 6242–6252 (2017).

50. M. G. Munowitz, R. G. Griffin, G. Bodenhausen, T. H. Huang, Two-dimensional rotational spin-echo nuclear magnetic resonance in solids: Correlation of chemical shift and dipolar interactions. *J. Am. Chem. Soc.* **103**, 2529–2533 (1981).

51. M. Hong, J. D. Gross, C. M. Rienstra, R. G. Griffin, K. K. Kumashiro, K. Schmidt-Rohr, Coupling amplification in 2D MAS NMR and its application to torsion angle determination in peptides. *J. Magn. Reson.* **129**, 85–92 (1997).

52. A. Bielecki, A. C. Kolbert, M. H. Levitt, Frequency-switched pulse sequences: Homonuclear decoupling and dilute spin NMR in solids. *Chem. Phys. Lett.* **155**, 341–346 (1989).

53. M. W. Maciejewski, A. D. Schuyler, M. R. Gryk, I. I. Moraru, P. R. Romero, E. L. Ulrich, H. R. Eghbalnia, M. Livny, F. Delaglio, J. C. Hoch, NMRbox: A resource for biomolecular NMR computation. *Biophys. J.* **112**, 1529–1534 (2017).

54. A. Vangone, A. M. Bonvin, Contacts-based prediction of binding affinity in protein-protein complexes. *eLife* **4**, e07454 (2015).

55. Y. Shi, W. Zhang, Y. Yang, A. G. Murzin, B. Falcon, A. Kotecha, M. van Beers, A. Tarutani, F. Kametani, H. J. Garringer, R. Vidal, G. I. Hallinan, T. Lashley, Y. Saito, S. Murayama, M. Yoshida, H. Tanaka, A. Kakita, T. Ikeuchi, A. C. Robinson, D. M. A. Mann, G. G. Kovacs, T. Revesz, B. Ghetti, M. Hasegawa, M. Goedert, S. H. W. Scheres, Structure-based classification of tauopathies. *Nature* **598**, 359–363 (2021).

56. Y. Wang, O. Jardetzky, Probability-based protein secondary structure identification using combined NMR chemical-shift data. *Protein Sci.* **11**, 852–861 (2002).